TECHNICAL UNIVERSITY OF CRETE

DIPLOMA THESIS

Development of a Cardiovascular Disease Monitoring System

Author:
Evangelos KATSOUPIS

Thesis Committee:
Prof. Michail ZERVAKIS
Prof. Euripides PETRAKIS
Prof. Michail G. LAGOUDAKIS

A thesis submitted in fulfillment of the requirements for the diploma of Electrical and Computer Engineer

in the

School of Electrical and Computer Engineering
Display Lab

Chania, July 2024

Πολυτεχνείο Κρήτης

Διπλωματική Εργασία

Ανάπτυξη Συστήματος Επιτήρησης για Καρδιολογικές Παθήσεις

Συντάκτης:
Ευάγγελος Κατσούπης

Επιτροπή:
Καθηγητής Μιχάλης Ζερβάκης
Καθηγητής Ευριπίδης Πετράκης
Καθηγητής Μιχαήλ Γ. Λαγουδάκης

Μια διπλωματική εργασία που υποβλήθηκε για την απόκτηση του διπλώματος Ηλεκτρολόγου Μηχανικού και Μηχανικού Υπολογιστών

στη

Σχολή Ηλεκτρολόγων Μηχανικών και Μηχανικών Υπολογιστών
Εργαστήριο Ψηφιακής Επεξεργασίας Σήματος και Εικόνας

Χανιά, Ιούλιος 2024

Abstract

Cardiovascular diseases (CVDs) are the leading cause of death globally. Portable and wearable systems have increasingly been used for the real-time acquisition and analysis of human electrophysiological activity. In this regard, these systems have been adopted for monitoring cardiovascular diseases, demonstrating a potential for non-invasive diagnostics. However, these systems either rely on multicriteria-based methods, which are not data-driven, or are commercial products with limited access to performance assessment.

This thesis proposes an open-source, multi-sensor, portable system with real-time preprocessing, user-friendly monitoring, and a post-processing deep learning-based arrhythmia detector (CVD index) with related electrocardiogram (ECG) features. The use of Movesense Medical multisensory device attached to a chest belt is capable of capturing medical grade, 1-lead ECG at various sampling rates. A Raspberry Pi 4 is the processing platform, providing the necessary computational power for signal processing and device communication. To facilitate communication with the sensing device, a wrapper API was developed and the Dash framework was used to create the user interface for communication and monitoring.

Various algorithms were employed and benchmarked to clean the signal and detect ECG morphological features, such as R-peaks, RR intervals, ECG-derived respiration, heart rate and its variability metrics. The extracted ECG morphological features were combined with time-frequency representations (derived from Continuous Wavelet Transform - CWT) for training a convolutional neural network (CNN) to detect arrhythmia types, according to the Association for the Advancement of Medical Instrumentation standards. The MIT-BIH Arrhythmia Database was used to train the detection model, employing and comparing various signal processing techniques and different CWT wavelets.

A low-energy consumption and portable system was assembled having the unique opportunity of acquiring and analyzing cardiac activity. For the arrhythmia detection module, an open source database of 44 patients with an overall of 110.000 labeled heartbeats (normal/abnormal). A median filter followed by a notch filter, and the use of the Gaussian 4 derivative mother wavelet (GAUS4), were applied as the preprocessing steps. The preprocessed signals were then used for training/testing purposes of the adapted CNN, leading to high overall accuracy and F1 scores at different classes (SVEB-80.75%, VEB-93.90%), surpassing those results reported in similar studies. The presented cardiac monitoring and arrhythmia detection system enables accurate and timely intervention in cardiovascular health monitoring.

Περίληψη

Οι καρδιοαγγειακές παθήσεις είναι η κύρια αιτία θανάτου παγκοσμίως. Φορητά και φορετά συστήματα χρησιμοποιούνται όλο και περισσότερο για την απόκτηση και ανάλυση βιοσημάτων σε πραγματικό χρόνο. Σε αυτό το πλαίσιο, τέτοια συστήματα έχουν υιοθετηθεί για την παρακολούθηση των καρδιοαγγειακών παθήσεων, επιδεικνύοντας δυνατότητες για μη επεμβατική διάγνωση. Ωστόσο, τα εν λόγω συστήματα, είτε βασίζονται σε πολυκριτήριες μεθόδους, οι οποίες δεν βασίζονται σε δεδομένα, είτε είναι εμπορικά προϊόντα, με περιορισμένη πρόσβαση στην αξιολόγηση των επιδόσεων.

Η παρούσα διπλωματική εργασία προτείνει ένα πολυαισθητηριακό, φορητό και ανοικτού τύπου κώδικα σύστημα, φιλικό προς τον χρήστη, κάνοντας πιο εύκολη την παρακολούθηση και ανιχνευτή αρρυθμιών, βασισμένο σε μοντέλο βαθιάς μάθησης, εκπαιδευμένο σε χαρακτηριστικά ηλεκτροκαρδιογραφήματος (ΗΚΓ). Γίνεται χρήση της συσκευής Movesense Medical, η οποία τοποθετημένη σε ζώνη στήθους, είναι ικανή να καταγράφει ιατρικής ποιότητας, μονοκαναλικό ΗΚΓ σε διάφορους ρυθμούς δειγματοληψίας. Το Raspberry Pi 4 χρησιμεύει ως πλατφόρμα επεξεργασίας, παρέχοντας την απαραίτητη υπολογιστική ισχύ για την επεξεργασία σημάτων και την επικοινωνία με τη συσκευή. Για να πραγματοποιηθεί η επικοινωνία με τον αισθητήρα, αναπτύχθηκε μια βοηθητική βιβλιοθήκη και για να δημιουργηθεί το γραφικό περιβάλον για την διεπαφή χρήστη με την πλατφόρμα επεξεργασίας και την συσκευή καταγραφής έγινε χρήση της βιβλιοθήκης Dash.

Διάφοροι αλγόριθμοι χρησιμοποιήθηκαν και αξιολογήθηκαν για την επεξεργασία του σήματος και την ανίχνευση χαρακτηριστικών μορφολογίας ΗΚΓ, όπως παλμοί R, τα χρονικά διαστήματα RR, η εκτίμηση αναπνοής που προκύπτει από το ΗΚΓ, ο καρδιακός ρυθμός και διάφοροι δείκτες μεταβλητότητας αυτού. Τα εξαγόμενα μορφολογικά χαρακτηριστικά συνδυάστηκαν με αναπαραστάσεις χρόνου-συχνότητας (που προέρχονται από τον συνεχή μετασχηματισμό με wavelet - CWT) για την εκπαίδευση ενός συνελικτικού νευρωνικού δικτύου για την ανίχνευση τύπων αρρυθμιών, σύμφωνα με τα πρότυπα της ένωσης Association for the Advancement of Medical Instrumentation standards (AAMI). Η Βάση Δεδομένων MIT-BIH Arrhythmia χρησιμοποιήθηκε για την εκπαίδευση του μοντέλου ανίχνευσης, χρησιμοποιώντας και συγκρίνοντας διάφορες τεχνικές επεξεργασίας σήματος και διαφορετικά κύματα CWT.

Ένα σύστημα χαμηλής κατανάλωσης ενέργειας και φορητότητας συναρμολογήθηκε, προσφέροντας τη δυνατότητα απόκτησης και ανάλυσης της καρδιακής δραστηριότητας. Για το μοντέλο ανίχνευσης αρρυθμιών, χρησιμοποιήθηκε μια ανοικτή βάση δεδομένων 44 ασθενών με συνολικά 110.000 ετικετοποιημένους καρδιακούς παλμούς. Εφαρμόστηκαν ως βήματα προεπεξεργασίας, φίλτρο μεσαίας τιμής ακολουθούμενο από φίλτρο notch και χρήση του μητρικού wavelet Gaussian 4ης παράγωγου (GAUS4). Τα προεπεξεργασμένα, πλέων σήματα, χρησιμοποιήθηκαν στη συνέχεια για την εκπαίδευση/δοκιμή του προσαρμοσμένου CNN, οδηγώντας σε υψηλή συνολική ακρίβεια, αλλά και F1 scores σε διάφορες κλάσεις

(SVEB-80.75%, VEB-93.90%), ξεπερνώντας τα αποτελέσματα που αναφέρθηκαν σε παρόμοιες μελέτες. Το παρουσιαζόμενο σύστημα παρακολούθησης καρδιάς και ανίχνευσης αρρυθμιών επιτρέπει ακριβή και έγκαιρη παρέμβαση στην παρακολούθηση της καρδιοαγγειακής υγείας.

Acknowledgements

I would like to convey my appreciation to the Technical University of Crete community for the invaluable assistance and resources, which were instrumental in completing this journey.

I am deeply grateful to my supervisor, Professor Michail Zervakis and *Dr. Marios Antonakakis*, for their unwavering support and guidance throughout this process, the numerous discussions we made, the insightful overviews they gave, and their consistent support.

A special thanks to the committee members, Professors Euripides Petrakis and Michael G. Lagoudakis, for the time they dedicated to reviewing my work, as well as to the new people I met at the DISPLAY lab.

I am also grateful to all my friends, both old and new, for the various moments, support, and time we have shared.

Most importantly, I would like to express my deepest thanks to my family for their unwavering support throughout this journey, despite the challenges that arose.

Thank you all!

Contents

Abstract i

Περίληψη iii

Acknowledgements v

Contents vi

List of Figures viii

List of Abbreviations x

1 Introduction 1
- 1.1 Motivation and Innovation . . . 1
- 1.2 Objective . . . 2
- 1.3 Structure . . . 2
- 1.4 Acknowledgment . . . 3

2 Theoretical Background 4
- 2.1 Human Heart and Arrhythmias . . . 4
- 2.2 Biomedical Signal - ECG Processing . . . 5
- 2.3 ECG Morphology and Analysis Techniques . . . 9
  - 2.3.1 Morphology . . . 9
  - 2.3.2 Real Signal Preproccesing . . . 11
    - Median Filtering . . . 12
    - Notch Filtering . . . 13
    - Butterworth filtering . . . 16
  - 2.3.3 RR intervals . . . 18
  - 2.3.4 ECG-Derived Respiration . . . 21
  - 2.3.5 Heart Rate Variability . . . 22
  - 2.3.6 Continuous Wavelet Transform . . . 25
- 2.4 Arrhythmias . . . 29
- 2.5 Machine Learning . . . 29
  - 2.5.1 Convolutional Neural Network . . . 30
  - 2.5.2 Metrics . . . 32

3 Requirements and Specifications of System **36**
3.1 Overview . . . 36
3.2 Hardware Interface and Embedded Systems . . . 37
3.2.1 Microprocessor . . . 37
3.2.2 Sensing Device . . . 37
3.3 Software Interface . . . 38
3.3.1 Communication With The Sensor . . . 38
3.3.2 Graphical User Interface . . . 40
3.3.3 Arrhythmia Detection Module . . . 41
Overview . . . 41
Dataset . . . 42
Preprocessing . . . 42
CNN Model and Training Setting . . . 46

4 Results **48**
4.1 CNN metrics . . . 48
4.2 SVM Metrics . . . 50
4.3 Selected Model . . . 50
4.4 R Peak Algorithm Comparison . . . 52
4.5 Applications . . . 54
4.6 Hardware . . . 58

5 Discussion **60**
5.1 Outlook . . . 65
5.1.1 Device Communication and GUIs . . . 65
5.1.2 Arrhythmia Model Training . . . 66

Bibliography **67**

List of Figures

2.1 Human Heart . . . 5
2.2 Einthohoven triangle . . . 6
2.3 Normal 12-lead ECG . . . 7
2.4 Electrocardiographic leads . . . 8
2.5 ECG QRS Complex . . . 9
2.6 Sample ECG . . . 11
2.7 Sample ECG Heartbeat . . . 12
2.8 Median Filtered ECG . . . 13
2.9 Frequency Spectrum of Sample ECG . . . 13
2.10 Frequency response of notch filter . . . 14
2.11 Frequency Response After Notch Filtering . . . 15
2.12 ECG Spectrogram After Notch Filtering . . . 15
2.13 Zoomed Heartbeats After Notch Filtering . . . 16
2.14 Butterworth Filter Orders . . . 16
2.15 ECG Filters . . . 18
2.16 ECG Filters On Heartbeat . . . 18
2.17 Pan et al. QRS detection workflow . . . 19
2.18 Hamilton et al. QRS detection workflow . . . 20
2.19 Rodrigues et al. QRS detection workflow . . . 21
2.20 Neurokit Default QRS detection workflow . . . 21
2.21 EDR display . . . 23
2.22 Mother Wavelets . . . 28
2.23 CWT For Each Wavelet . . . 28
2.24 Confusion Matrix . . . 33

3.1 App Pipeline . . . 36
3.2 GATT Diagram . . . 39
3.3 CNN Pipeline . . . 41
3.4 Noisy and Abnormal ECG and CWT . . . 44
3.5 Abnormal ECG and CWT . . . 44
3.6 Abnormal Heartbeat and CWT . . . 45
3.7 Abnormal Heartbeat and CWT . . . 45
3.8 Abnormal Heartbeat and CWT . . . 46

4.1 R-Peak Algorithm Accuracy I . . . 52

4.2 R-Peak Algorithm Accuracy II 52
4.3 R-Peak Detection Time by Algorithm and Database I 53
4.4 R-Peak Detection Time by Algorithm and Database II 53
4.5 Capture And Processing App 54
4.6 Sensor Communication Example 54
4.7 Capturing ECG Example 55
4.8 Preparing to Process the ECG 55
4.9 Initial State Of Analytics Display App 56
4.10 Scanning Results of Display App 56
4.11 Snapshot of the Display App (I) 57
4.12 Snapshot of the Display App (II) 57
4.13 Arrhythmias Sample Visualization 57
4.14 Movesense Medical 58
4.15 Raspberry Pi 4 B 58
4.16 Whaveshare Monitor 59
4.17 3D Case 59

List of Abbreviations

WS	**W**earable and portable **S**ystems
CVD	**C**ardio**V**ascular **D**iseases
HR	**H**eart **R**ate
ECG	Electro**C**ardio**G**ram
LA	**L**eft **A**tria
RA	**R**ight **A**tria
LV	**L**eft **V**entricular
RV	**R**ight **V**entricular
RRI	**R** peak - **R** peak **I**nterval
IIR	**I**nfinite **I**mpulse **R**esponse
EDR	**E**CG-**D**erived **R**espiration
HRV	**H**eart **R**ate **V**ariability
ULF	**U**ltra **L**ow **F**requency
VLF	**V**ery **L**ow **F**requency
LF	**L**ow **F**requency
HF	**H**igh **F**requency
VHF	**V**ery **H**igh **F**requency
CWT	**C**ontinuous **W**avelet **T**ransform
MEXH	**Mex**ican **H**at Wavelet
MORL	**MORL**et Wavelet
GAUSP	**Gaus**sian **P** Deritive Wavelet
AAMI	**A**ssociation for the **A**dvancement of **M**edical **I**nstrumentation
N	**N**ormal class of AAMI
SVEB	**N**ormal class of AAMI
VEB	**N**ormal class of AAMI
Q	Unknown beats class of AAMI
ML	**M**achine **L**earning
CNNs	**C**onvolutional **N**eural **N**etwork**s**
MLP	**M**ulti **L**ayer **P**erceptron
SVM	**S**upport **V**ector **M**achines
TP	**T**rue **P**ositive
FP	**F**alse **P**ositive
TN	**T**rue **N**egative
FN	**F**alse **N**egative

BLE	**B**luetooth **L**ow **E**nergy
BLEAK	**B**luetooth **L**ow **E**nergy platform **A**gnostic **K**lient
ACC	**Acc**elerometer
MAGN	**Magn**etometer
GYRO	**Gyro**scope
IMU	**I**nertial **m**easurement **U**nit
GUI	**G**raphical **U**ser **I**nterface
BPM	**B**eats **P**er **M**inute
GATT	**G**eneric **ATT**ribute Profile
EEG	**E**lectro**E**ncephalo**G**raphy

Chapter 1

Introduction

1.1 Motivation and Innovation

Cardiovascular diseases (CVDs) are responsible for the most deaths globally, causing around 17.9 million fatalities each year. This extensive group includes a range of heart and blood vessel disorders, such as coronary heart disease, cerebrovascular disease, rheumatic heart disease, and other related conditions. Due to the considerable influence of CVDs on worldwide well-being, it is essential to give priority to monitoring overall heart health. Integrating non-invasive monitoring systems is crucial in detecting risks early and taking proactive steps to manage heart health, ultimately decreasing the likelihood of severe cardiovascular events.

Non-invasive monitoring systems offer a practical and efficient solution for continuous heart health tracking without the need for complex and intrusive procedures. These devices can capture critical heart metrics, providing individuals with valuable insights into their cardiovascular health.

A multitude of solutions and products have been proposed to address this need. For example, the Apple Watch [2] is a widely used wearable that includes electrocardiogram capabilities and irregular rhythm notifications, like the ones when sensing episodes of atrial fibrillation, bradycardia, or tachycardia offering users feedback on potential heart issues in general. Similarly, Garmin watches and Garmin software [26] are known for their robustness and the use of a range of sensors and features for health-tracking metrics. While they offer features like continuous heart rate monitoring and can alert users to unusually high or low heart rates, they cannot capture detailed arrhythmias like an electrocardiogram device. Another widely use device is the Samsung watches [73]. Again, it provides a comprehensive set of health monitoring features, including the ability to capture electrocardiograms and detect arrhythmias like atrial fibrillation and abnormalities in heart rate.

However, these devices are intended to complement professional medical advice and should not replace consultations with healthcare providers. A medical-grade solution should be considered, the Corsano wearables and software [17]. Their medical-grade solution is designed to provide detailed health and wellness insights,

particularly useful in clinical settings and health monitoring for general purposes as well as chronic conditions. Their ability to provide various health metrics and detect abnormalities in the medical grade recordings, note it as a good solution with the only drawback the monthly subscription they need.

Given the limitations of existing solutions where either the range of information is limited and not medical-grade or the cost is prohibitively high, the proposed solution leverages a medical-grade single-lead electrocardiogram device integrated with a Raspberry Pi microcontroller. This setup allows users to capture and process their electrocardiogram recordings with high precision, enabling them to monitor various heart health metrics and detect multiple types of arrhythmias. The system offers significant advantages, including low cost, low energy consumption, and the potential for future upgrades. By using a Raspberry Pi, users gain the flexibility to tailor data processing and analysis to their needs, providing a comprehensive and customizable approach to heart health monitoring.

1.2 Objective

This thesis aims to design, develop, and validate a non-invasive multisensory system for cardiac health monitoring using a medical-grade device called Movesense Medical, software for signal processing and analytics representation, and an embedded system that serves as the processing unit. The system integrates with an application to provide a user interface for sensor connectivity, real-time data capture and later on processing and anomaly detection. Additionally, a separate application was developed to display a variety of detected arrhythmias and other relevant ECG metrics for monitoring purposes, providing insights into heart and body health. The proposed system has the potential to improve personalized medicine and clinical practices by providing a smart, low-cost and low energy consumption portable device, capable of monitoring and informing users about their cardiac health.

1.3 Structure

This work will start by diving into the theoretical background needed, following a general-to-specific pattern. The study will begin by analyzing the significance of the ECG readings, the features that can be extracted from them, and some of the processing techniques used. Then, the reader can investigate the different types of arrhythmias and approaches to capturing these events, including machine learning techniques, one of which is used for the proposed system. In Chapter 3, the study design on which this work is based is introduced and explained in depth, starting with the choice of the processing unit, the multisensor device, and later the software used to integrate the above. Additionally, the ECG preprocessing techniques will be discussed, both for the captured data and for the features that can be extracted

from it. Later on, the machine learning pipeline will be reviewed to understand how the arrhythmia detection model works and what its performance is. Finally, the framework used to integrate the above and present them to the user will be discussed, leading to Chapter 4 where the whole system is analyzed. This study concludes with some discussion on the above and the possible future work that can be done.

1.4 Acknowledgment

This work used equipment from the Display Lab of the Technical University of Crete, which was bought with the support of the Ideas Incubator carrier and the project "Actions of Academic Innovation within the Framework of the Innovative Entrepreneurship Observatory of the Region of Crete". The equipment consists of a custom 3D-printed case, custom-designed to hold the Raspberry Pi, its power unit, and a Waveshare touch display for the graphical user interface. The 3D printing of the case's design was carried out using the printers provided by the TUC Innovation Lab.

Chapter 2

Theoretical Background

2.1 Human Heart and Arrhythmias

The human heart is one of the main organs in our cardiovascular system, primarily responsible for circulating blood throughout the circulatory system in the human body. The heart consists of four chambers, with the left and right atria, the receiving chambers, located in the upper segment and the left and right ventricles, the expelling chambers, located at the lower part of it. In a healthy heart, a continuous circle occurs when the right atrium receives deoxygenated blood from the circulatory system and passes to the right ventricle, which then expels it to the lungs through the pulmonary circulation, where it receives oxygen and gives off carbon dioxide. [69] The oxygenated blood returns to the left atrium, moves into the left ventricle and is then pumped out through the aorta into the systemic circulation. As the blood travels through the body, it exchanges nutrients, oxygen, and other substances with carbon dioxide before returning to the right atrium ([11, 43, 69]).

This entire process is controlled by the contractions of the heart, regulated by a group of pacemaker cells located in the sinoatrial node, a cluster of myocytes in the upper wall of the right atrium near the opening of the superior vena cava (figure 2.1). These cells generate an electric current that is distributed through the cardiac conduction system, causing the heart to contract and produce the known heartbeat rhythm. In a healthy individual, this occurs at a rate of approximately 60 to 100 times per minute. The heart's electrical activity can be monitored using an electrocardiogram (ECG), a well-established diagnostic tool that captures the heart's electrical changes, with the use of electrodes, over time. More details about the ECG will be discussed later.

When a disturbance in the regularity, the site of origin or conduction of the cardiac electric system happens, an **arrhythmia** event occurs. During an arrhythmia event, the heart rate may increase (tachycardia), decrease (bradycardia) or follow an irregular and/or abnormal rhythm such as the case of atrial fibrillation where atrial pulses become unsynchronized [4]. While most arrhythmias are harmless, in some cases the heart may not be able to pump enough blood leading to a lack of blood flow and disturbing the health of many vital organs like the brain the heart itself and

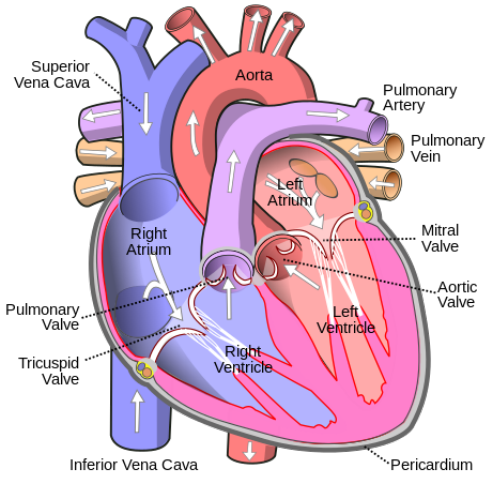

FIGURE 2.1: Representation of the Human Heart

other organs too. Some are non-life-threatening and only medical attendance and therapy are required. However, life threatening ones can cause heart failure and/or sudden death if not correctly attended. Thus, continuous monitoring of the health of the heart and cardiac arrhythmias is crucial, as it can potentially prevent severe complications and improve a patient's overall health.

2.2 Biomedical Signal - ECG Processing

Biological signals, or biosignals, can be defined as the spatial, temporal, or spatio-temporal records of biological events, such as muscle contractions during movement, electrical reactions of the brain during sleep (like the dream stage), or, in our case, the beating of the heart. During a biological event, electrical, chemical, and mechanical activities result in signals that can be measured and examined. To read these types of data, devices and mechanics are needed to measure, evaluate, and treat biological systems [61]. This type of engineering is known as bioinstrumentation or biomedical instrumentation and its main aspect is monitoring a biological species' physiological parameters with a variety of sensors. Some common biosignals can be measured by using:

- Electroencephalography (EEG): brain electrical activity signal recordings
- Electromyography (EMG): muscle contractions signal recordings
- Electrooculography (EOG): eye signal recordings
- Electrocardiography (ECG): heart signal recordings

In this study, we will focus on reading human electrocardiograms how they can get processed and what features can be extracted from them.

Willem Einthoven, a Dutch scientist, created a galvanometer in 1901 that was capable of capturing the electrical activity of the heart. He discovered that when action potentials propagate between negatively and positively charged electrodes, a trace can be generated. As noted in [5], after discovering that tracings differed depending on where the positive and negative electrodes were placed, he described three angles, or leads, that formed a triangle with the heart in the center. The current term for this is Einthoven's triangle, and the primary limb leads I, II, and III are the names given to the three electrode configurations (figure 2.2) It is worth noting that the third electrode serves as the ground of the current.

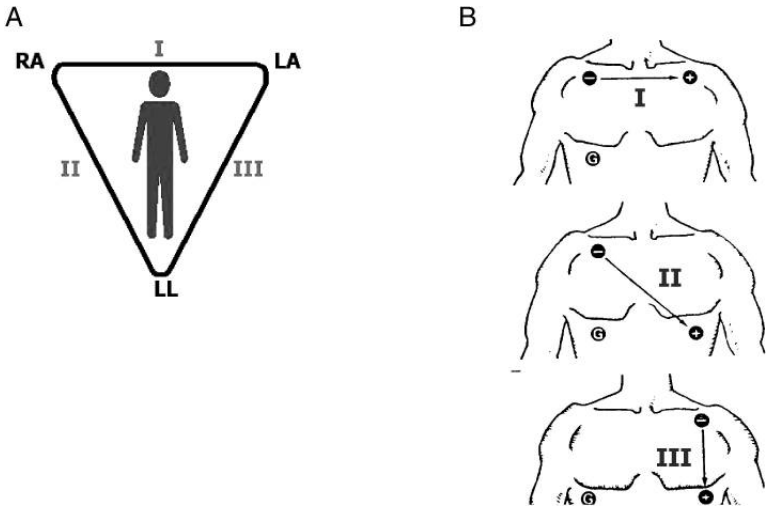

FIGURE 2.2: A) EinthohovenTriangle, B) standard limb leads I, II, and III.

After the 20th century, researchers' further work allowed doctors to examine electrical events as they propagate in multiple ways through the heart, similar to how an apple slicer divides an apple into different portions. These days, the cardiologist uses a 12-lead ECG analysis to help diagnose multiple heart related diseases as well as complicated arrhythmias.

Specifically electrocardiogram, or ECG [57], records from the surface of the body, with the use of electrodes and measures the variations in electrical potential that the heart produces. The heart's cells create action potentials, and the order in which they activate determines the signal that is recorded. Also, the recorded signal is alternated by numerous cardiac and extracardiac variables like the heart's location within the body, the kind of tissue separating it from the other vascular organs as well as the position of the recording electrode. All the above affect or get affected by the electrical forces the heart produces and thus the sensor reads. So, ECG records do not offer the exact anatomic or physiologic characteristics of the heart but the difference in the electrical dynamic the electrodes receive, which is alternated by the noted heart characteristics. To link the electrocardiogram patterns with the actual

heart events, clinicians and researchers had to precisely correlate the ECG recordings with observable anatomic, pathologic, and physiologic data, to lead them to the understanding of how the state of the heart is represented.

Continuing by understanding what is an ECG record, traditional ECG recordings refer to the machine that makes electric activity measures by drawing a trace on a moving electrocardiograph paper [57]. As shown in figure 2.3, it consists of 12 leads or different records obtained by ten electrodes which are placed at different parts of the body. Explaining figure 2.4 the corresponding leads and their readings, as well as the image of the heart they receive (in parentheses), are:

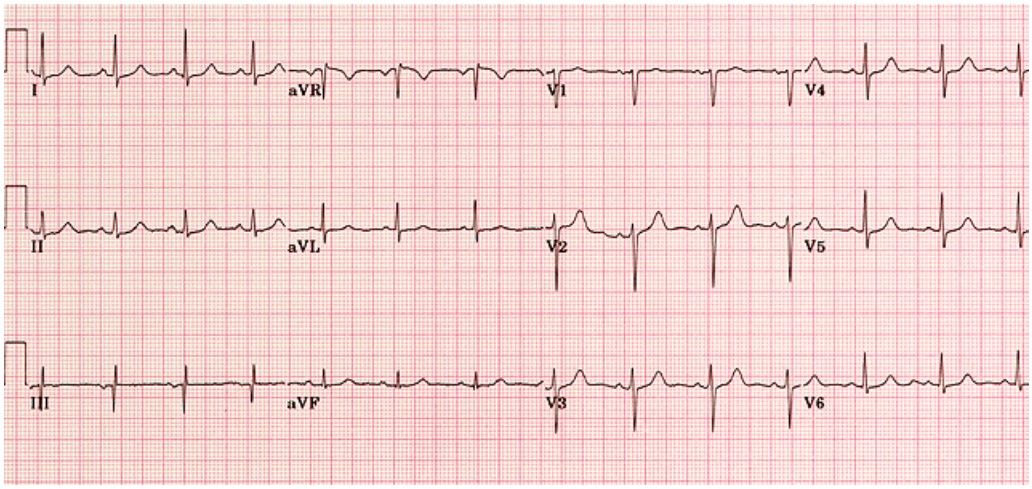

FIGURE 2.3: Normal 12-lead ECG.

- Bipolar Leads proposed by Einthohoven:
  - Lead I: The potential difference between the left arm and right arm, with the left arm as the positive pole (left side of the heart).
  - Lead II: The difference in potential between the right arm and left leg, with the left leg serving as the positive pole (inferior left view).
  - Lead III: The differences in potential between the left arm and left leg, with the left leg as positive (inferior right view).
- Augmented Unipolar Leads that record the potential between arms or leg, and the lead formed by summing the other two unused limb leads, as ground. The leads and their corresponding readings are:
  - Lead aV**R**: The difference of potential between the **R**ight arm and the summing of the leads of the left arm and leg, with the right arm serving as the positive pole (upper right side).

- Lead aV**L**: The difference of potential between the **L**eft arm and the summing of the leads of the leg and the right arm, with the left one as the positive pole (upper left view).
- Lead aV**F**: The difference of potential between the **F**oot and the addition of the arms' leads, with a positive pole on the leg (hearts inferior wall).

Combining the unipolar and the bipolar leads can gather the cardiac electrical vectors of the entire frontal plane (360°).

- Chest Leads or the precordial leads, that are placed on the front and the lateral chest, capture part of the horizontal plane. Each one of them stands as the positive pole and as the negative, the one is formed by electrically connecting all the limb leads. Namely:
  - Lead V1: Fourth right intercostal space adjacent to the sternum (view oriented to right ventricle).
  - Lead V2: Fourth left intercostal space adjacent to the sternum (V1).
  - Lead V3: Midpoint of a line connecting V2 and V4 (inter ventricular septum view).
  - Lead V4: Fifth left intercostal space in the midclavicular line (same as V3).
  - Lead V5: Same level as V4 on the anterior axillary line (left ventricle anterolaterally view).
  - Lead V6: Same level as V4 and V5 on the midaxillary line (same as V5).

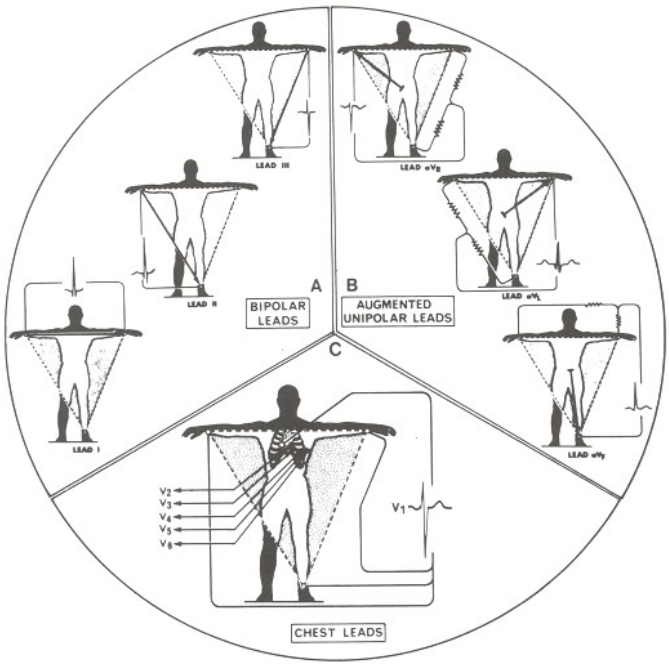

FIGURE 2.4: Electrocardiographic leads and heartbeats they record.

This way, when an electrical current moves toward one of the chest leads and gets recorded, it will be deflected as an upward deflection. On the contrary, the electrical current or the vector, defined as the current, that moves on the right side of the chest, will be recorded as a negative spike in the left anterior precordial lead.

Knowing the above, it is almost assured that the information obtained from ECG findings accurately simulates the heart's real behavior, making it easier to extract features that provide useful information on the ways of its normal functions and, most importantly, on how it behaves in abnormal states such as arrhythmias.

2.3 ECG Morphology and Analysis Techniques

2.3.1 Morphology

Analyzing a normal person's heartbeat morphology from an ECG measurement, as noted earlier, can lead to findings that refer to the health, activity status and condition of the heart. Some of the most important features can be shown at figure 2.5 where a record part of a normal heartbeat is segmented to its morphological features like peaks and their duration [14].

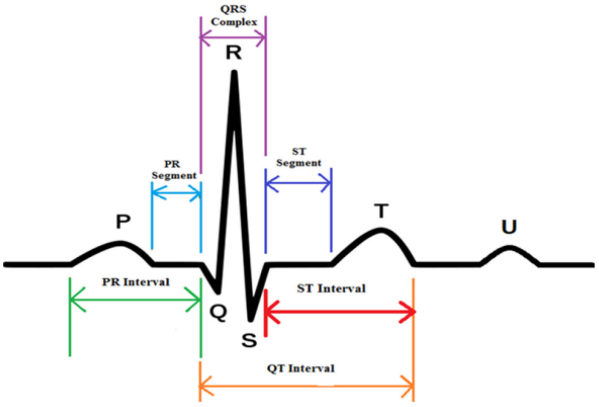

FIGURE 2.5: Different segments of one heartbeat.

The primary components are P-wave, QRS complex, T-wave, and the interval between them. The periodic activation, or depolarization, of the left and right atria (LA, RA), is what causes the P-wave, followed by the appearance of the QRS complex, which is caused by the right and left ventricular (LV, RV) depolarization like the simultaneous activation of the left and right ventricles. Ventricular re-polarization raises T-waves and after their depolarization, the U-wave follows. Information is also carried by the intervals between waves. The time needed between the beginning of ventricular depolarization (QRS complex) and the beginning of atrial depolarization (P-wave) produces the PR interval. While the QT interval is dependent on the length of ventricular depolarization and repolarization, the QRS period is dependent only on the depolarization of the ventricular muscle. The period (or rate)

of the atrial and ventricular cycles, respectively, determines the PP and RR intervals. A more detailed summarization of the wave types can be found in table 2.1 and 2.2

TABLE 2.1: Detailed morphological features of waves in normal ECG.

Wave Type	**Duration (s)**	**Amplitude (mV)**	**Remarks**
P-wave	$0.08 - 0.12$	0.25	Depolarization of LA & RA [35]
Q-wave	0.03	$0.2 - 0.4$	Initial ventricular depolarization [1]
R-wave	–	1.6	Depolarization of the ventricles [40, 45]
S-wave	–	$1.8 - 3.0$	Final ventricular depolarization [45]
T-wave	$0.1 - 0.25$	$0.1 - 0.5$	Ventricular repolarization [48]
U-wave	–	$0.1 - 0.33$	Re-polarization of heart's conduction system [48]

TABLE 2.2: Detailed morphological features of intervals in normal ECG.

Interval Type	**Duration (s)**	**Amplitude (mV)**	**Remarks**
PR	$0.12 - 0.20$	120	Atrial & ventricular depolarization [49]
QRS	$0.06 - 0.12$	$2.5 - 3.0$	Depolarization of ventricles [3, 20]
QT	$0.35 - 0.44$	–	Reflect ventricular repolarization [94]
RR	$0.6 - 1.2$	–	Measures heart rate variability [44]
PP	$0.60 - 1.04$	–	Interval between two P-waves [35]
ST (segment)	0.08	$0.1 - 0.2$	Early repolarization [38]

2.3.2 Real Signal Preproccesing

Knowing the morphology of a healthy heartbeat, we can assume a real single lead (lead II) ECG recording, like the one in figure 2.6.

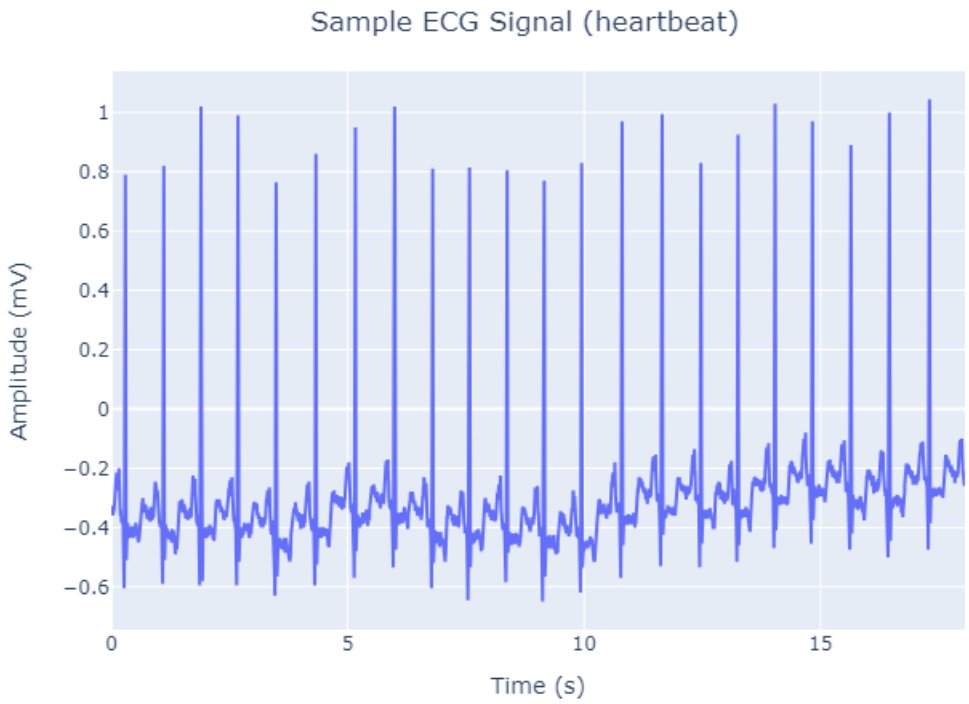

FIGURE 2.6: Raw ECG signal.

By now, we can see several variations in the amplitude, like the one of the sifting on the negative scale. Also, if focused on a single heartbeat (figure 2.7), and compared with the quality features of the ones of figure 2.5, except the P wave and QRS complex the other features are not noticeable. This occurs due to various noises and artifacts that obscure critical details about the heart's electrical activity. One of them is known as *baseline wander*, which can be linked to respiratory activity and respiration, as well as abrupt bodily motion and electrode motion artifacts. For example, due to the baseline wanders frequency content commonly being in the range of 0 to 0.5 Hz, the ST–T segment can be interfaced with subtle changes [19], as well as it appears to 'wander' or move up and down rather than be straight. Another type is the power line interface, a signal in the frequency of 50 or 60 Hz and bandwidth below 1 Hz [42]. This interference matches the frequency of the local electrical power system (60 Hz in North America and 50 Hz in most of Europe) and is imposed on signal measurement systems like the one of ECG. Therefore, the received signal has to be preprocessed by filtering to reduce noise artifacts while preserving the heartbeat's quality features. Several techniques, employed in this study, are detailed and analyzed below.

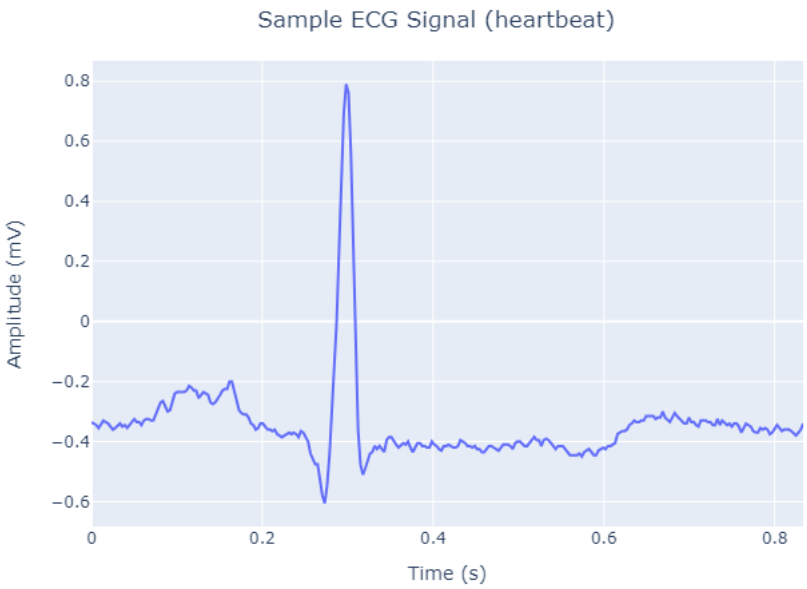

FIGURE 2.7: Segment of a heartbeat from figure 2.6.

Median Filtering

In general, the median of a group of numbers is the value that separates the higher half from the lower half of a numeric array, representing the middle value of the dataset. The *median filter* is a common non-linear filtering method used to eliminate noise in images and, in our case, signals. The concept is that it iterates through the signal, entry by entry, substituting each entry with the median of the entry and its neighboring entries, This approach is similar to a moving average filter, where each value is replaced with the average of itself and its adjacent values. Let us call the number of the length of the neighborhood n. The "window" of length n describes the arrangement of neighboring units that move across the complete signal. The mathematical model of the median value $\tilde{k}$ of an array $\boldsymbol{X}$ is :

$$\textbf{Med}\,(\boldsymbol{X}) = \tilde{k} = \begin{cases} \boldsymbol{X}\left[\frac{n+1}{2}\right] & \text{if } n \text{ is odd} \\ \frac{\boldsymbol{X}\left[\frac{n}{2}\right]+\boldsymbol{X}\left[\frac{n}{2}+1\right]}{2} & \text{otherwise} \end{cases} \tag{2.1}$$

Following the work of [14], two median filters were used, one with a sliding window of length $n = 200ms$ and one with the length of $n = 600ms$. The first median filter was used to remove QRS complexes and P-waves, while the $600ms$ filter applied to the $200ms$ one was used to remove the T waves. The second filter operation generated a signal with the ECG signal baseline, which was later subtracted from the original one to create the baseline-corrected ECG signal. The advantage of this type of filtering is that it neatly removes outliers while adding no phase distortion. The raw signal, its baseline noise and the final one can be shown in figure 2.8.

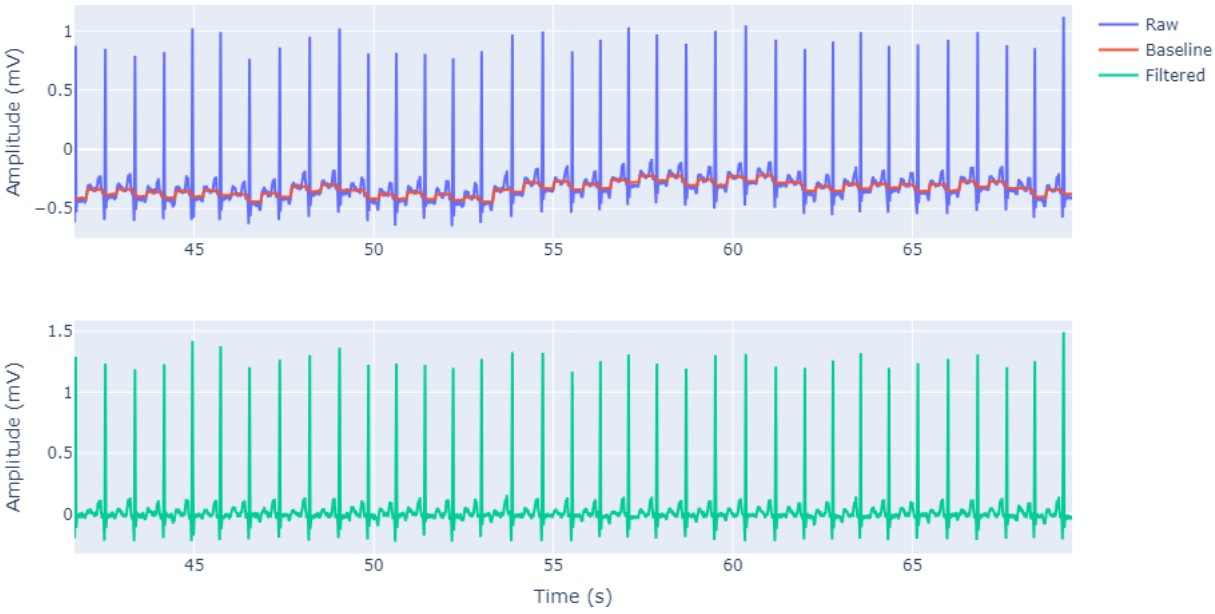

FIGURE 2.8: At the top, the sample raw signal with its baseline noise. At the bottom, is the filtered sample signal.

Notch Filtering

By converting the ECG signal to the frequency domain with methods like Fourier Transform [23], and knowing that the power line can disturb the ECG reading occurring a spike at 50 or 60 Hz and harmonics at multiples of the power line's frequency but at match lower magnitude, can be detected both on the original raw signal and the baseline removed one (figure 2.9).

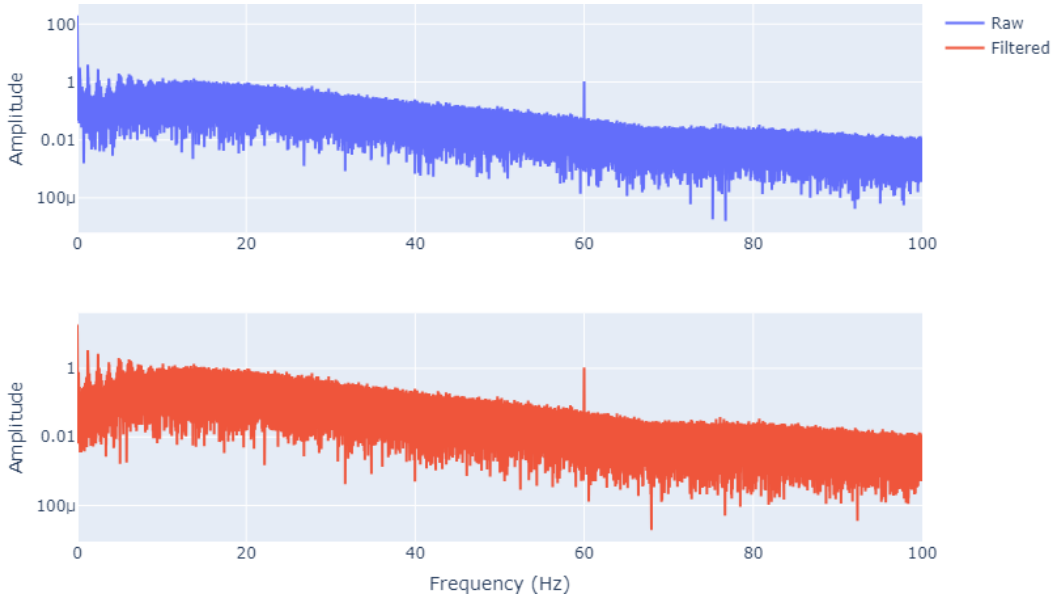

FIGURE 2.9: At the top, the frequency domain of the sample raw signal. At the bottom, is the frequency domain of the baseline free sample signal. Both signals hold the US-based power line noise.

It is noticeable the impact of the baseline removal as the most significant changes are in the low frequencies, where the wanders frequency content commonly occurs. Investigating the spike at 60 Hz (the sample is US-based), an IIR notch filter [12, 65] is used to reject a single frequency component of noise. Mathematically, the IIR filter is characterized by the recursive equation 2.2,

$$y[n] = \sum_{k=0}^{\inf} h[k]x[n-k] = \sum_{k=0}^{N} b_k x[n-k] - \sum_{k=1}^{M} a_k y[n-k] \tag{2.2}$$

Where, $h[k]$ is the filter impulsive response that it has an infinite value, and a_k, b_k are the filter coefficients. The $x[n]$ and $y[n]$ are the input and the output of the filter. The transformation of 2.2 to the Z-domain [52] produce the transfer function of it and is a sequence of real or complex numbers, into a complex valued frequency domain is shown at 2.3, where $z_{1:N}$ and $p_{1:M}$ are the zeros and the poles of $H(z)$, used to calculate coefficients of notch filters.

$$H[z] = \frac{b_0 + b_1 z^{-1} 1 + \ldots + \ldots + b_n z^{-N}}{1 + a_1 z^{-1} + \ldots + a_M z^{-N}} = \frac{\sum_{k=o}^{N} b_K z^{-k}}{1 + \sum_{k=1}^{M} a_K z^{-K}} \xrightarrow{factorization}$$

$$H[z] = \frac{K\,(z - z_1)\,(z - z_2)\ldots(z - z_N)}{(z - p_1)\,(z - p_2)\ldots(z - p_M)} \tag{2.3}$$

Figure 2.10 shows the behavior of the previously mentioned filter, with an emphasis on the frequency we want to isolate.

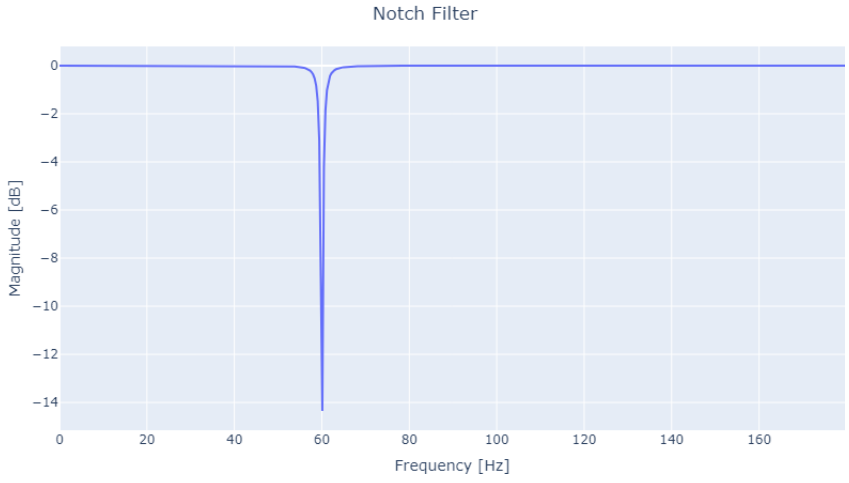

FIGURE 2.10: Frequency response of notch filter in where the well is at the desired rejected frequency.

If we apply the filter to the signals of 2.11, we can see that the 60 Hz spike and a small frequency neighborhood reduced. The result is more noticeable at figure 2.13 where raw and median filtered heartbeats are compared with the ones after the notch filtering.

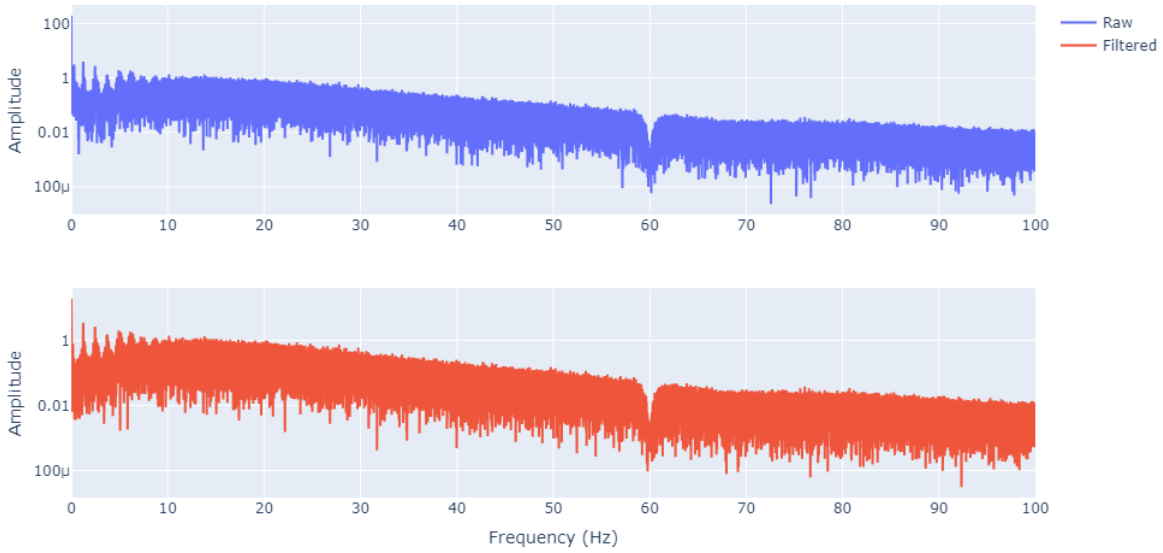

FIGURE 2.11: Frequency response of the notch filtering for raw and median filter signal.

A more detailed presentation of the notch filter impact can be viewed in the scaleograms of figure 2.12. Scaleogram is a way of visualizing the change of a signal's frequency content over time after applying a short-time fourier transform. The 60 Hz power line noise is visible in the raw ECG and removed in the filtered one. Additionally, it is important to note the presence of the harmonic frequency at 120 Hz, which has a lower intensity than the 60 Hz noise as well as, the noticeable among the overall frequency components, of the ECG.

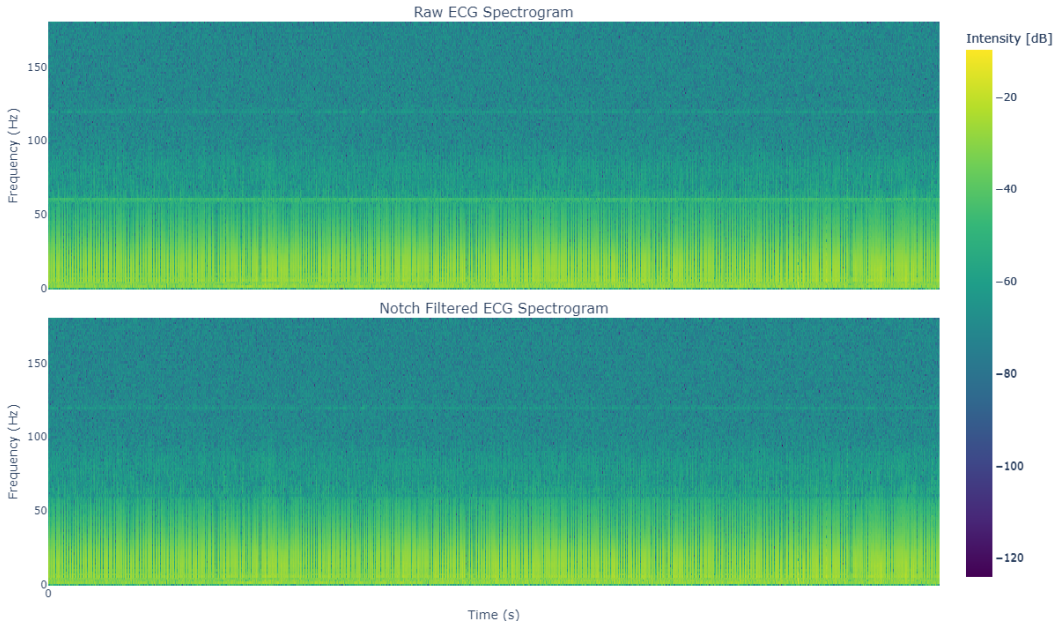

FIGURE 2.12: The spectrograms of the whole raw ECG signal (top) and after notch filtering (bottom) at the frequency of 60 Hz.

Finally, one can perceive that the variation produced by the power line frequency (60 Hz) is smoothed without differentiating the morphological characteristics of the signals.

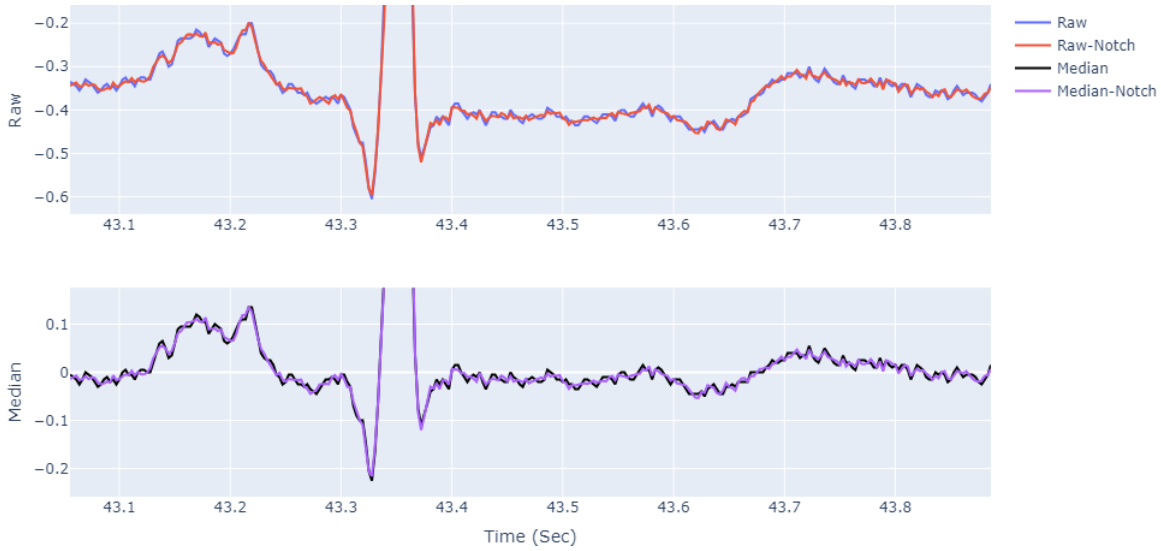

FIGURE 2.13: Zoomed in version of 2.7 after power line frequency removal. At the top, the raw heartbeat and the notched one. At the bottom, the median filtered heartbeat before and after notch filtering.

Butterworth filtering

A signal processing filter designed to have as flat as possible frequency response, followed by a gradual rejection of unwanted frequencies, called a butterworth filter.

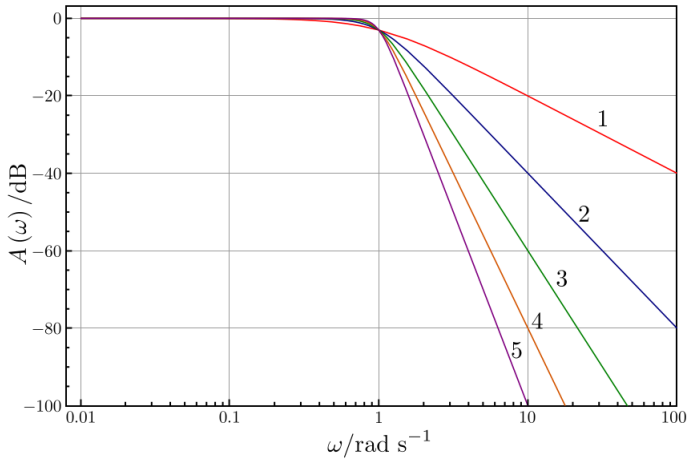

FIGURE 2.14: Plot of the gain of Butterworth low-pass filters of orders 1 through 5.

The $n-th$ order transfer function is the 2.4,

$$H[s] = G_0 \prod_{k=1}^{n} \frac{\omega_c}{s - s_k} \tag{2.4}$$

whereas s_k are the zeros of the product of the denominator, G_0 the signal's gain at zero frequency, ω_c, the cutoff frequency and $s = j\omega$ [76]. At figure 2.14 we can see the gain and the flat response of different orders of a low-pass butterworth filter. Worthy to note that other types of this family of filters (high-pass, band-pass, etc), have a similar quality of gain and response.

Some more of the cleaning filters used in this study are listed below:

- Neurokit [51]
  The default cleaning method of the *NeuroKit2* pythons toolbox uses an 5_{th} order highpass butterworth filter with cutoff frequency at 0.5 Hz (baseline wanders central frequency) to remove slow drift and DC offset on the given signal, followed by powerline noise removing filter by smoothing the signal with a moving average kernel with the width of one average window with the width of power lines frequency (not recommended for 60 Hz power line systems).

- Pan & Tompkins [59]
  The cleaning technique used by the QRS detection algorithm proposed by Pan et al. in 1985, uses a variation of a 1_{st} order bandpass butterworth filter with cutoff frequencies at 5 and 15 Hz, where in this range lie the most significant features of the ECG.

- Elgendi [21]
  The use of a 2_{nd} order band pass butterworth filter with cutoff frequencies at 8 and 25 Hz proved to produce good quality signals.

To understand the impact of the above filter techniques, figure 2.15 displays the 'cleaned' signals in contrast with the raw one and figure 2.16 displays the impact of them on a single heartbeat. In every case, the baseline wanderer is reduced, as well as the ripple effect, but in the techniques of Pan Tompkins and Elagandi the morphological distortion is intense. The reason for this will be discussed in the next subsection.

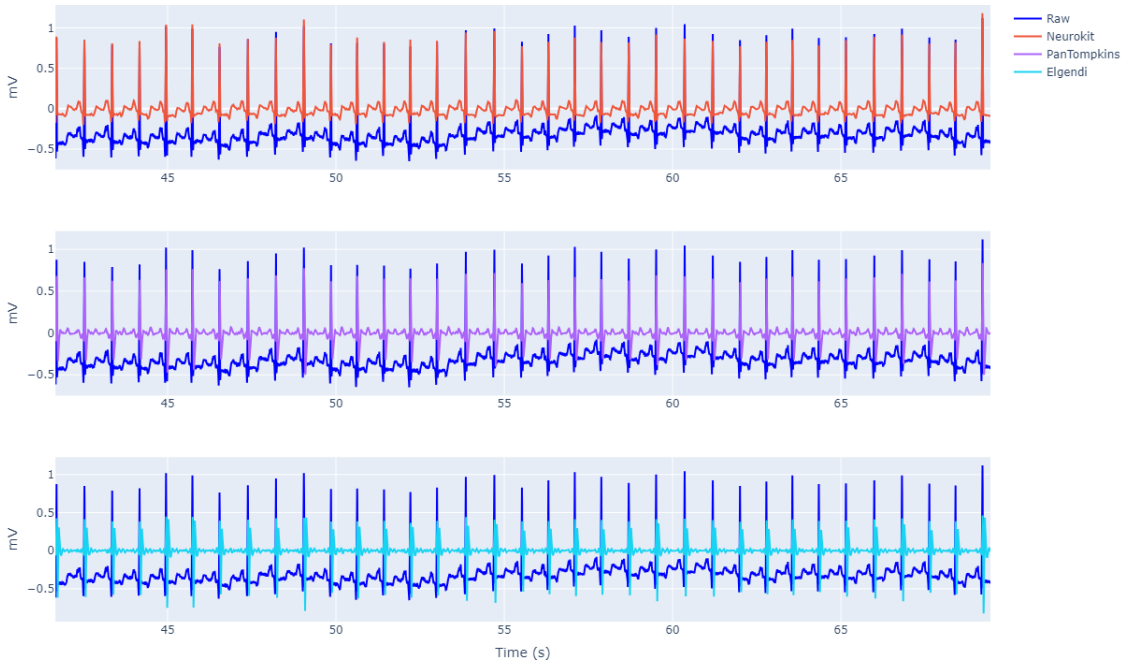

FIGURE 2.15: Impact of Neurokit, PanTompikns, and Elgandis filtering techniques on the raw ECG

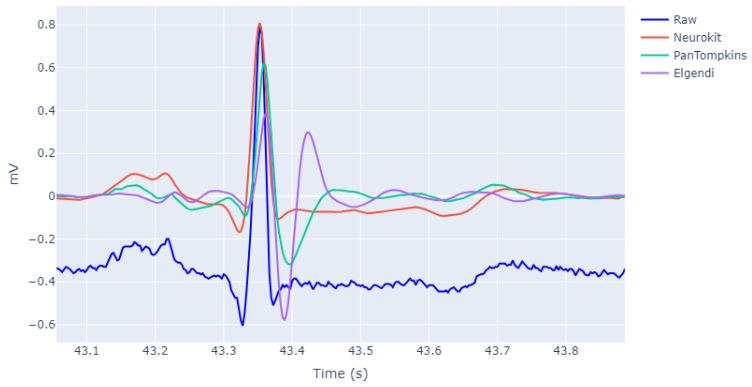

FIGURE 2.16: Impact of Neurokit, PanTompikns, and Elgandis filtering techniques on the single heartbeat.

2.3.3 RR intervals

The feature of the series of time intervals between successive QRS complex R peaks presented in the ECG is called the RR Interval (RRI) series of the corresponding signal and has its one statistical properties. Directly correlated to the RR series, is the heart rate, which is the average number of complete heartbeats in a specific section of time (usually minutes), because it is derived from the frequency of the RRI. Generally, a shorter RRI indicates a higher heart rate, while a longer one suggests a lower heart rate. Having an ECG signal, somehow we have to find where the QRS complexes are and more specifically where the R peaks are located in the hole signal. For these, several techniques were implemented to solve this problem, and every one of

them has its one approach.

- Pan and Tompkins [59]
  The algorithm first filters the signal through both a low pass and a high pass filter to minimize the impact of muscle noise, power line interference, baseline wander, and T-wave interference. Following the previous description of signal cleaning using the same name cleaning technique, the signal is differentiated to provide the QRS slope information.

  Next, the signal is squared point by point to convert all data points into positive values and highlight the higher frequencies, and then the algorithm uses sliding window integration to gather waveform feature data to hold the temporal location of the QRS complex. At the final step, Two thresholds are fine-tuned. The upper of the two thresholds is used to detect peaks in the signal. The lower threshold is utilized in cases where the higher threshold fails to detect any peaks within a specific time frame. In this situation, the algorithm must look back in time to find a missing peak.

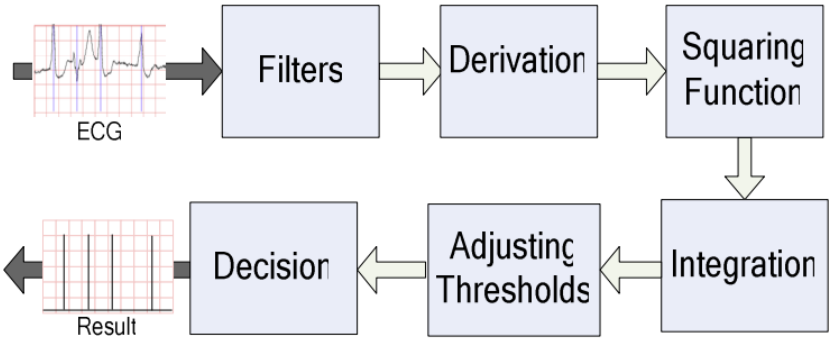

FIGURE 2.17: Graphical representation of the basic steps of Pan and Tompkins [62].

- Hamilton [31]
  The process involves preprocessing the ECG signal through bandpass filtering with cut-off frequencies at 8 and 16 Hz. Later, the negative values of the filtered signal are converted to positive through the rectification process to give better sensitivity. An average sliding window is applied to detect the complexes but in contrast with the previous technique, a QRS complex detection rule is followed. Finally, using estimates of QRS peaks and noise peak heights, the detection threshold is calculated. Namely, the rules are:

  – any peaks detected within 200 milliseconds before or after more prominent peaks are disregarded.

  – If the peak is detected, and it does not contain both positive and negative peaks, it represents a baseline shift, so it gets rejected.

- If a peak occurs 360 ms after the previous peak with a maximum slope lower than 50 % of the previous peak's slope, it is considered to be a T-wave.
- If the detected peak surpasses the detection threshold, are categorized as QRS complexes, otherwise, consider it as noise.

.

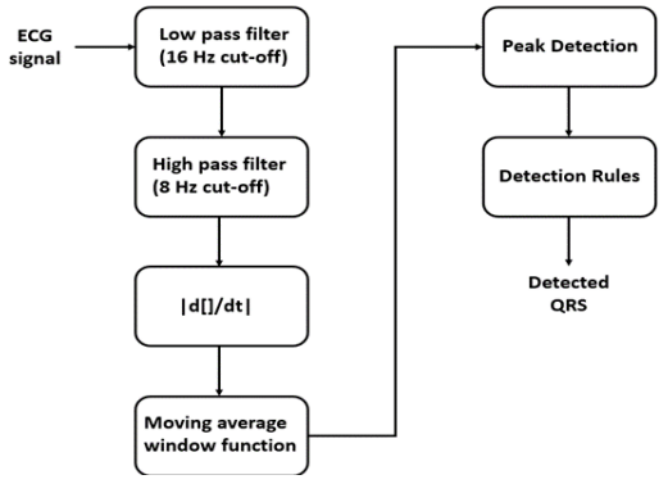

FIGURE 2.18: Graphical representation of the basic steps of Hamilton algorithm [39].

- Rodrigues [70]
  The Rodrigues algorithm processes ECG signals by initially designating the first ten seconds as the learning stage and the following three-second intervals as detection stages. The incoming signal is resampled to 80 Hz and subjected to a 2-level Stationary Wavelet Transform [24] using the Daubechies 3 ('db3') as the mother wavelet. This setup, including the three-second detection stage and the chosen wavelet, optimally performs across multiple signals from various ECG databases. After applying the wavelet transform, the detail coefficients from the second level are extracted, squared, and then smoothed using moving window averaging. The resultant signal is normalized to a [0, 1] range, enhancing the peaks around the QRS complexes and reducing other amplitudes to nearly zero, which helps in accurately identifying the R-peak locations, albeit with a slight delay.

  These normalized peaks are utilized to compute thresholds for beat-to-beat intervals and R-peak amplitudes, aiding in the detection of beats in subsequent three-second ECG segments. The algorithm continuously monitors the six most recent beats to calculate the standard deviation of the five most recent RR intervals. This metric assists in identifying varying heart rate activities,

allowing the algorithm to adjust thresholds appropriately for detecting premature beats, atrial fibrillation, and other arrhythmias like ventricular tachycardia. However, our algorithm does not detect ventricular fibrillation beats, and such beats were excluded from the performance evaluation.

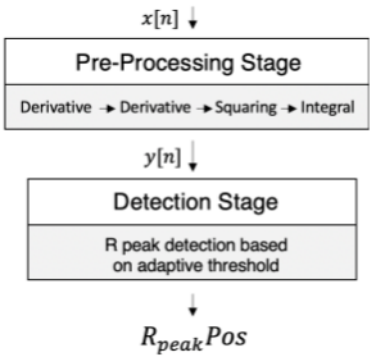

FIGURE 2.19: Graphical representation of the basic steps of Rodrigues algorithm [70].

- Neurokit [9, 51]
  The proposed method of the neurokit toolbox starts by smoothing the ECG signal and its first derivative (the gradient) using a window averaging technique, to remove high-frequency noise and emphasize the QRS complexes. Next, the algorithm identifies the start and end points of the QRS complexes by finding the points where the smoothed gradient exceeds a threshold witch is calculated based on the average of the smoothed gradient. Then it iterates through each QRS complex, identifying the local maxima within each complex. These local maxima correspond to the peaks of the QRS complex. To not misidentify false peaks, a minimum delay is enforced between each peak, ensuring that there is a sufficient time interval between consecutive peaks.

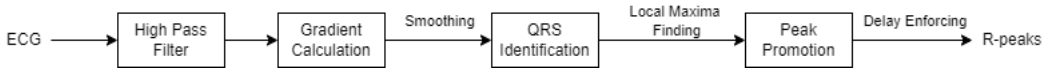

FIGURE 2.20: Graphical representation of the basic steps of Nuerokit's toolbox default peak detection method.

2.3.4 ECG-Derived Respiration

Another feature that can be extracted from the ECG signal, is the ECG-Derived Respiration (EDR), a proxy of a respiratory signal based on heart rate. With only one sensor, ECG and respiration signal monitoring can be done simultaneously, being less intrusive for the patient and more comfortable and economical, due to the reduced number of wires and sensors used. The general idea before the extraction of

the proxy respiration is the breathing patterns from heart rate data, which are calculated from the RRI data. During inhalation, heart rate tends to increase and at the exhalation stage, tends to decrease [30], a piece of information that allows for calculating an estimate of the breathing rate from signals of the heart rate. In this study, 3 different methods were used to compute respiration signals from EDR data. All of them are based on bandpass butterworth filtering at low frequencies. This is a result of the frequency band of the respiration slow signal, which generally is in the range of 0.1-0.7 Hz (one respiration cycle can be derived from ECG corresponds to 4-10 heartbeats).

TABLE 2.3: Methods for EDR signal extraction.

Method	low cutoff (Hz)	high cutoff (Hz)	Remarks
HeartPy implementation [88]	0.1	0.4	Difference between the ground truth and the estimated rates at 0.028 (Mean) & 0.015 (Median).
Sarkar et al. work [74]	0.1	0.7	Mean Absolute Error (MEA) between true and estimated respiration peaks at $\pm$0.028.
Charlton et al. study [10]	0.066	1	Comparison and combination of 314 algorithms.

All methods shown in Table 2.3 and represented in Figure 2.21 produce results with similar morphology.

2.3.5 Heart Rate Variability

Another widely used feature, that can be obtained from ECG recordings and more specifically from the RRI series, is Heart Rate Variability (HRV). In contrast with HR, which is the number of heartbeats per minute, HRV refers to the variation in the time intervals between consecutive heartbeats [78]. Generally, HRV is created through interactions between the heart and brain, as well as complex non-linear autonomic nervous system processes, and assesses neurocardiac function. It is the property that emerges from regulatory systems working together on various time scales to assist in adapting to environmental and psychological challenges. HRV indicates control of autonomic balance and includes regulation of blood pressure, gas exchange, gut, heart, vascular tone, and potentially facial muscles [75].

Non-linear systems' variability, like the oscillations of a healthy heart, allows them to quickly adjust to unpredictable and changing surroundings. Disease can reduce or escalate complexity, contrasting with the spatial and temporal complexity seen

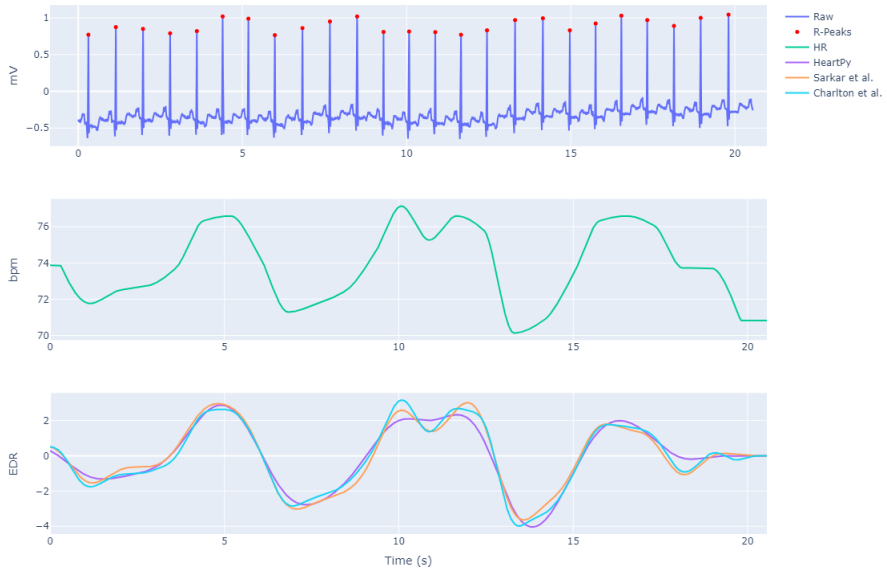

FIGURE 2.21: Representation of the computed EDR signals (bottom) in respect of the HR data (middle) in respect of the RRI of the sample ECG (top).

in healthy biological systems. For example, elevated HRV measurements due to cardiac conduction abnormalities are strongly correlated with higher mortality risk, especially in the elderly. This indicates that increased HRV may not always be favorable as medical conditions can also cause it.

Following the studies of [64, 77], HRV can be described using the time domain, frequency domain, and non-linear measurements and are analyzed below.

- Time Domain Metrics
  Time domain measures of HRV evaluate the level of diversity in inter beat interval measurements, representing the time gap between consecutive heartbeats. These values can be presented in their original units or converted to natural logarithms to achieve more normally distributed data [84]. The overall HR variability is representing and is not specific in determining the individual impacts of various regulatory mechanisms. Nonetheless, this overall sensitivity can be viewed as a beneficial characteristic, such as in preliminary research or when not focusing on particular neuropsychological mechanisms. Furthermore, time-domain measures remain widely reported HRV indices due to their simple calculation and understanding.

- Frequency Domain Metrics
  Frequency-domain measurements estimate the distribution of absolute or relative power into four frequency bands that the HR is oscillating. The bands are ultra low frequency (ULF), very low frequency (VLF), low frequency (LF), high

TABLE 2.4: HRV Time-Domain Metrics.

Metric	**Remarks**
MeanNN	The mean of the RR intervals.
SDNN	Standard deviation of RR intervals.
SDANN(1,2,5)	Standard deviation of average RR intervals extracted from 1,2 or 5 minute segments of time series data.
SDNNI(1,2,5)	The Mean of Standard deviation of average RR intervals extracted from 1,2 or 5 minute segments of time series data.
RMSSD	Root mean square of successive RR interval differences.
SDSD	The standard deviation of the successive differences between RR intervals.
CVNN	SDNN divided by the MeanNN.
CVSD	RMSSD divided by the MeanNN.
MedianNN	The median of the RR intervals.
MadNN	The median absolute deviation of the RR intervals.
MCVNN	MadNN divided by MedianNN.
IQRNN	The interquartile range (IQR) of the RR intervals.
SDRMSSD	SDNN divided by the RMSSD.
Prc(20 - 80NN	The 20th or 80th percentile of the RR intervals.
pNN(20 - 50)	The proportion of RR intervals greater than 20 or 50 ms, out of the total number of RR intervals.
MinNN	The minimum of the RR intervals.
MaxNN	The maximum of the RR intervals.
TINN	Baseline width of the RR interval histogram or a geometrical parameter of the HRV.
HTI	The HRV triangular index or the total number of RR intervals divided by the height of the RR intervals histogram

frequency (HF) and very high frequencies (VHF) bands. The spectral powers for each frequency and more are displayed at table 2.6.

TABLE 2.5: HRV Frequency-Domain Metrics.

Metric	Remarks
ULF	The energy of ultra low frequencies ($\leq 0.0033\ Hz$).
VLF	The energy of very low frequency band ($0.0033 - 0.04\ Hz$).
LF	The energy of low frequency band ($0.04 - 0.15\ Hz$).
HF	The energy of high frequency band ($0.15 - 0.4\ Hz$).
VHF	The energy of very high frequency band ($0.4 - 0.5\ Hz$).
TP	The total spectral power
LFHF	LF divided by HF.
LFn	The normalized LF, calculated by dividing it by TP.
HFn	The normalized HF, calculated by dividing it by TP.
LnHF	The log-transformed HF.

- Non Linear Measurements. Nonlinear indices encompass characteristics extracted from the Poincaré plot, a visual depiction showing each RR interval plotted against its preceding RR interval, enabling us to measure the randomness of a time series.

2.3.6 Continuous Wavelet Transform

Another method that is used not only for feature extraction but also for overall signal processing is the so called wavelet transformation [18, 79–83, 87]. In the wavelet transform family exists a lot of types of transforms, with the most mentioned being the continuous wavelet transform (CWT), the discrete wavelet transforms as well as the stationary discrete wavelet transform. This section aims to provide an understanding of the CWT method which is used in this study. Generally, wavelet transforms of a signal are derived by comparing the input signal with stretched and moved variations of the original wavelet, known as the mother wavelet. Because of their short duration, return two dimensional results, providing information in the frequency as well as in time domain, making them ideal for describing events that have distinct beginnings and endings, such as non-stationary signals like the one of ECG [47].

Let's assume the given signal $x(t)$, which is going to transform via CWT. The inner product of $x(t)$ with a mother wavelet $\psi(t)$ produce the transforms coefficients as:

TABLE 2.6: HRV Frequency-Domain Metrics.

Metric	**Remarks**
S	Area of the ellipse, which represents HRV ($SD1 \cdot SD2 \cdot \pi$).
SD1	standard deviation perpendicular the line of identity.
SD2	standard deviation along the line of identity.
SD1/SD2	Ratio of SD1 to SD2 that describes the ratio of short term to long term variations in HRV.
ApEn	Approximate entropy, which measures the regularity and complexity of a time series.
SampEn	Sample entropy, which measures the regularity and complexity of a time series.
DFA $\alpha 1$	Detrended fluctuation analysis characterizes short-term changes in value.
DFA $\alpha 2$	Detrended fluctuation analysis characterizes long-term changes in value.
D_2	Correlation dimension calculates the fewest variables needed to create a model of system dynamics.

$$CWT[x(t)] = X_w(a,b) = \frac{1}{|\alpha|^{1/2}} \int_{-\infty}^{\infty} x(t)\tilde{\psi}\left(\frac{t-b}{a}\right) dt \tag{2.5}$$

where $\alpha \in \mathbb{R}^{+*}$ is the scale of the transform which causes the dilation of the wavelet, $b \in \mathbb{R}$ the translational value, which causes the shifting of it and $\tilde{\psi}(t)$ the dual function of the wavelet $\psi(t)$. Due to the properties of the Fourier transform, 2.5 can be displayed as the convolution of the given signal $x(t)$ and the scaled and mirrored wavelet:

$$CWT[x(t)] = X_w(a,b) = |\alpha|^{-1/2} \left(x(b) * h_\alpha(b)\right) \tag{2.6}$$

where $h_\alpha(b)$, is the wavelet function $\psi(t)$ reversed in time and with complex conjugation applied for given α [8].

A variety of continuous mother wavelets have been proposed in the literature [67], with the most known being the mexican hat wavelet, the morlet wavelet, the complex morlet family of wavelets, gaussian and complex gaussian derivative family of

wavelets, shannon and frequency B-spline families. In this study, four of them were used and analyzed below.

- Mexican Hat Wavelet (MEXH)
  The Ricker or Mexican hat wavelet [72] is widely used in ECG processing wavelet and is given by equation 2.7, where the normalization factor in front is constant to ensure the wavelet has energy equal to one.

$$\psi(t) = \frac{2}{\sqrt{3}\sqrt[4]{\pi}} \cdot \exp^{\frac{-t^2}{2}}(1-t^2) \tag{2.7}$$

- Morlet Wavelet (MORL)
  The Morlet wavelet [6], is composed of a carrier of complex exponential, multiplied by a Gaussian window (envelope), as shown at 2.8.

$$\psi(t) = \exp^{\frac{-t^2}{2}} \cos(5t) \tag{2.8}$$

- Gaussian P Derivative Wavelets (GAUSP)
  The Gaussian wavelets ("gausP" where P is an integer between 1 and 8) correspond to the function 2.9, which is the Pth order derivative of the exponential function.

$$\psi(t) = \frac{d^P}{dt^P} \exp^{-t^2} \tag{2.9}$$

The above functions that are 2.22 are characterized as wavelets because their Fourier transform of $\psi(t)$ corresponds to a band-pass spectrum, whereas the scaling factor α determines its central frequency and bandwidth. Generally, a function, to consider a wavelet, must be square-integrable (a), must have a zero mean (b) and must satisfy the admissibility condition (c) [90].

$$a) \int_{-\infty}^{\infty} |\psi(t)|^2 dt < \infty\,, \quad b) \int_{-\infty}^{\infty} \psi(t)dt = 0\,, \quad C_\psi = 2\pi \int_{-\infty}^{\infty} \frac{|\hat{\psi}(\omega)|^2}{|\omega|} d\omega < \infty \tag{2.10}$$

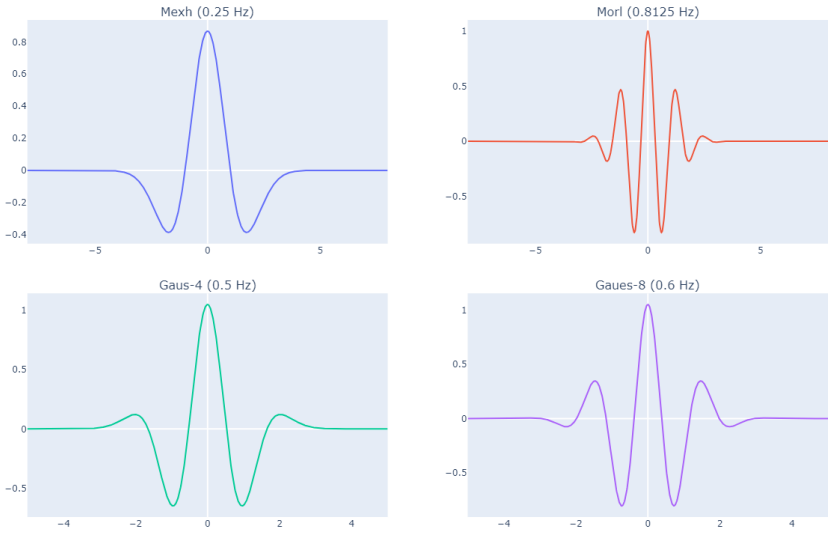

FIGURE 2.22: Mother wavelets and their central frequencies.

To understand better how each mother wavelet interphases with a given input signal, at figure 2.23 a sample input ECG signal is presented, as well as the scalograms of CWT with each wavelet. For the scalogram, the x-axis represents the time, y the scales used and the heat (colors) the absolute value (magnitude) of the wavelet coefficients obtained after performing CWT. Knowing the central frequency of each wavelet, we can translate each scale to the corresponding pseudo frequency of the signal, using the equation 2.11, where F_c is the central frequency of the wavelet used, s is the corresponding scale and F_s the sampling frequency.

$$F = \frac{F_c}{s} \cdot F_s \tag{2.11}$$

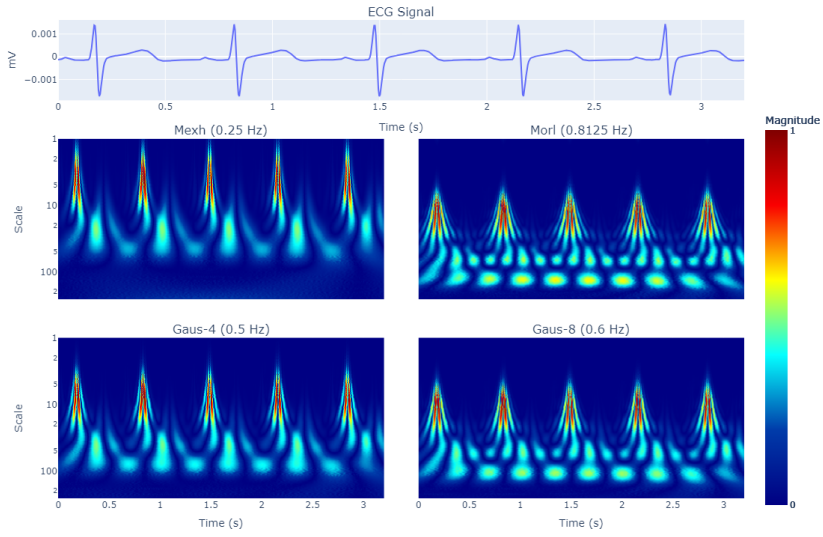

FIGURE 2.23: CWTs (log scale) of the ECG signal at various wavelets.

At each scalogram, we can see that at low frequencies or scales (normalized pseudo frequencies generated from the scales), the transform captures finer details and higher frequencies. However, the detailed analysis might not cover the entire signal duration because the wavelet is more localized in time (shorter), and captures the energy at the parts where the signal matches the scaled wavelet. At higher scales, with a stretched wavelet, broader features and lower frequencies are captured. This way, analysis cover the entire duration of the signal, but at the cost of losing some detail.

2.4 Arrhythmias

Knowing how to extract features of a healthy state heart, an abnormal one has to be discussed to understand the qualitative differences. As reported by the Association for Advancement of Medical Instrumentation (AAMI) [53, 54], there are 15 original types of heartbeats (healthy and abnormal) which are further categorized into five superclasses. Namely, these are:

- Normal (N).
  Normal class includes standard, healthy heartbeats occurring in a regular pattern.
- Supraventricular Ectopic Beats (SVEB).
  SVEB class includes the premature beats that originate in the atria as well as the ones with abnormal ventricular conduction and the ones that originate in the atrioventricular node. Also in this subset, the beats occurred by supraventricular tachycardia are accommodated.
- Ventricular Ectopic Beats (VEB).
  VEB class includes premature beats originating in the ventricles and the ones that occur by ventricular tachycardia.
- Fusion (F).
  Fusion beats that created by colliding and partially fusing two different electrical impulses.
- Unknown (Q).
  Refers to beats that cannot be confidently categorized into the other defined. Usually, these are paced beats or the fusion of them with normal ones.

The above categories can be viewed more specifically and detailed in table 2.7 where the widely known arrhythmia types matched the AAMI classes [15].

2.5 Machine Learning

To help scientists and doctors understand better the heart signal and classify the different types of morphological features like wave segments, metric features line

TABLE 2.7: AAMI heartbeat classes mapped to arrhythmia types.

AAMI Class	**N**	**SVEB**	**VEB**	**F**	**Q**
Description	Heartbeats not in SVEB, VEB, F, Q classes	Supraventricular ectopic beat	Ventricular ectopic beats	Fusion beat	Unknown Beats
	normal beat (NOR)	partial premature beat (AP)	premature ventricular contraction (PVC)	fusion of ventricular and normal beat (fVN)	paced beat (P)
	left bundle branch block beat (LBBB)	aberrated atrial premature beat (aAP)	Ventricular escape beat (VE)		fusion of paced and normal beat (fPN)
	right bundle branch block beat (RBBB)	nodal (junctional) premature beat (NP)			unclassifiable beat (U)
	atrial escape beat (AE)	supraventricular premature beat (SP)			
	nodal (junctional) escape beat (NE)				

HRV and EDR and overall the state the heart is (normal or arrhythmia), the field of machine learning is used. Machine Learning (ML) has arisen as a field in artificial intelligence, offering a novel method to address intricate issues. ML is the study of allowing computers to learn independently without being specifically programmed to do so, by creating algorithms that can learn from data and make predictions. Systems are allowed to evolve and enhance their performance by learning from more data, rather than being programmed for static tasks. This specific trait has enabled the completion of numerous tasks that were once deemed unfeasible or even unsolvable with set program commands. In this study, a subset model of ML is used to support the above aim and is called Convolutional Neural Networks (CNNs).

2.5.1 Convolutional Neural Network

Generally, CNNs [58] are known for their capability to automatically grasp spatial hierarchies of features from raw data, allowing them to detect local patterns, global structures, and semantic representations. To extract features from raw data various layers-methods are used, including convolutional layers, pooling layers, and fully connected layers. Kernels, also known as window filters, are convolved with input data in convolutional layers to extract important key points and generate feature maps. The pooling layers decrease the spatial dimensions of the feature maps, making the network better at handling translations and changes. In the end, the extracted features are combined with the fully connected layers to carry out the classification. Some more details for the layers used for the proposed study are:

- Convolution Layer.
  After the input is processed, the convolution layer, typically the initial layer of a CNN, convolves an image with a kernel of specific dimensions. Filters in CNNs are represented by small kernels applied to the data using a sliding window that moves across them, calculating the dot product between the data's

neighborhood and the kernel's values to generate a feature map of the input information.

- Batch Normalization.
  After the continuous extraction of the features map, their distribution may change, causing the training process to become slower and making the network more reliant on initial parameters. To deal with this problem, batch normalization [37] is used following the CNN layer to standardize the feature maps. This method regularizes the results from the convolutional layers to maintain a uniform average and dispersion. Through this action, batch normalization improves model performance by stabilizing the learning process which leads to faster convergence.

- ReLU Activation Function Layer.
  After the convolution and batch normalization steps, the activation function is applied. In this study, the activation function used is the known ReLU or rectified linear unit [46], which is defined by the function 2.12 where x is the input to the next convolution layer.

$$f(x) = max(0, x) \tag{2.12}$$

  This simple, yet effective operation introduces non-linearity into the model, enabling it to learn complex patterns. while it is computationally efficient, as it involves a straightforward shareholding operation.

- Max Pooling Layer.
  The max pooling layer [92] also referred to as the subsampling layer, is utilized to decrease the feature dimension and accelerate the training process. This process follows the ReLU activation layer, and its function is to compute the average or maximum convolution features among neighboring neurons in the preceding convolution layer.

The layers mentioned above work together to process raw data and identify various features that can be used in further computations to determine class scores in classification exercises. In our scenario, two processes utilized are known as multi-layer perceptron (MLP) and support vector machines (SVM). The MLP [86] is made up of connected layers that match extracted features to output classes by using non-linear activation functions to capture intricate patterns. On the contrary, SVMs [33] determine class scores by identifying ideal hyperplanes that divide various classes within the feature space. Both approaches utilize the feature extraction abilities of the layers before them to determine the probabilities of each feature for each class.

2.5.2 Metrics

Let us assume that we have trained a network with given data. To assess the accuracy and robustness of the employed network, it is essential to evaluate the model using labeled data not only during training to prevent weight overfitting but also to gauge its accuracy. Some of the widely used metrics [27] that help achieve these objectives are listed below.

- Confusion Matrix.
  The Confusion Matrix is a matrix that displays how well the model performs in classification tasks. In classification tasks, the outcome is an N x N matrix used for evaluating the performance of a classification model, where N is the number of target classes. As shown in figure 2.24 where $N = 2$ each cell holds one of the following:
  - True Positive (TP).
    The model correctly predicted a positive outcome (the actual outcome was positive).
  - False Positive (FP).
    The model incorrectly predicted a positive outcome (the actual outcome was negative).
  - True Negative (TN).
    The model correctly predicted a negative outcome (the actual outcome was negative).
  - False Negative (FN).
    The model incorrectly predicted a negative outcome (the actual outcome was positive).
- Accuracy.
  The overall model's performance is quantified using accuracy. It is the proportion of total accurate occurrences to the overall occurrences, as shown in equation 2.13.

$$Accuracy = \frac{TP + TN}{TP + TN + FP + FN} \tag{2.13}$$

- Precision.
  When dealing with a dataset with a skewed class distribution where the number of sample data of one class is much larger than others, accuracy alone is insufficient for evaluating the robustness of your model. For this reason, precision (equation 2.14) is used and it measures the accuracy of a model's positive predictions.

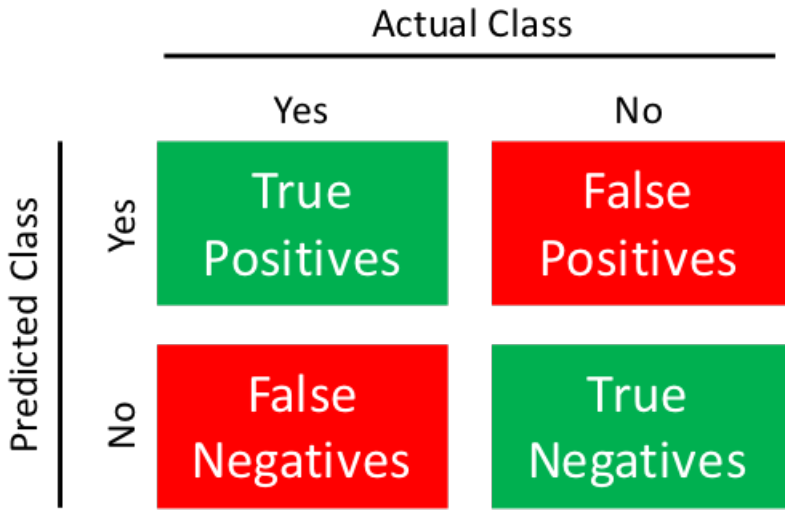

FIGURE 2.24: Confusion Matrix.

$$Precision = P = \frac{TP}{TP + FP} \tag{2.14}$$

- Recall.
  Recall, also known as sensitivity, is the measurement used to determine the amount of accurately predicted positive results compared to the total number of positive results. As this value approaches 1, the network is more likely to accurately identify most of the true positive frames. The equation that calculates the recall is the below.
  $$Recall = R = \frac{TP}{TP + FN} \tag{2.15}$$

- F1 score.
  The F1 score (equation 2.16) is a metric that combines precision and recall equally to calculate a harmonic mean or weighted average. The highest value of this metric is achieved at 1. and the lowest score achieved is 0. The goal of this metric is to strike a fair balance between precision and recall, a valuable tool when dealing with imbalanced datasets in a variety of situations.
  $$F1\ score = F1 = \frac{2 \cdot Precision \cdot Recall}{Precision + Recall} \tag{2.16}$$

When it comes to multi-class classification problems, the metrics mentioned above can offer insights into the model's performance for each class. For this reason, average and weighted metrics are used.

- Weighted Metrics.

Computes the metric for each class independently, but takes a weighted average based on the number of true instances of each class. This approach takes into account the balance of classes and is useful when there is an imbalance data set. So the above metrics are calculated like:

$$\textit{Weighted Precision} = \sum_{c=1}^{N} \frac{|C_c|}{\sum_{\tilde{c}=1}^{N} |C_{\tilde{c}}|} \cdot P_c \tag{2.17}$$

$$\textit{Weighted Recall} = \sum_{c=1}^{N} \frac{|C_c|}{\sum_{\tilde{c}=1}^{N} |C_{\tilde{c}}|} \cdot R_c \tag{2.18}$$

$$\textit{Weighted F1} = \sum_{c=1}^{N} \frac{|C_c|}{\sum_{\tilde{c}=1}^{N} |C_{\tilde{c}}|} \cdot F1_c \tag{2.19}$$

where $|C_c|$ is the number of true instances of class c, the sum $\sum_{\tilde{c}=1}^{N} |C_{\tilde{c}}|$ is the total number of true instances across all classes and P_c, R_c, $F1_c$ the recession, recall and f1-score for each class.

- Average Metrics.
  The average metrics are separated into micro and macro averages. Macro average computes the metric independently for each class and then takes the mean of those metrics. It treats all classes equally, regardless of their size. The equations given them are 2.23 to 2.25 where N is the total number of classes.

$$\textit{Macro } P_c = \sum_{c=1}^{N} \frac{P_c}{N} \tag{2.20}$$

$$\textit{Macro } R_c = \sum_{c=1}^{N} \frac{R_c}{N} \tag{2.21}$$

$$\textit{Macro } F1_c = \frac{1}{N} \sum_{c=1}^{N} \frac{2 \cdot \textit{Macro } P_c \cdot \textit{Macro } R_c}{\textit{Macro } P_c + \textit{Macro } R_c} \tag{2.22}$$

  On the other hand, the micro average calculates the metric globally by counting the total true positives, false positives, and false negatives across all classes. Metrics are extracted by making calculations using these global counts.

$$\textit{Micro } P = \frac{\sum_{c=1}^{N} TP_c}{\sum_{c=1}^{N} TP_c + FP_c} \tag{2.23}$$

$$\textit{Micro } R = \frac{\sum_{c=1}^{N} TP_c}{\sum_{c=1}^{N} TP_c + FN_c} \tag{2.24}$$

$$\textit{Micro } F1_c = \frac{1}{N} \sum_{c=1}^{N} \frac{2 \cdot \textit{Micro } P_c \cdot \textit{Micro } R_c}{\textit{Micro } P_c + \textit{Micro } R_c} \tag{2.25}$$

Overall, macro-averaging computes precision, recall, and F1 scores for each class separately and then averages them across all classes. This method gives the same

weight to every class, regardless of their size or the amount of examples they have. On the other hand, micro-averaging calculates the total counts of true positives, false positives, and false negatives for all classes and uses these totals to determine the overall metric. This approach gives equal consideration to every instance, irrespective of its class, ensuring all predictions have equal importance in the final metric evaluation. Both macro- and micro-averaging offer perspectives on model performance across classes, with the former concentrating on metrics for individual classes and the latter highlighting performance across all predictions.

Chapter 3

Requirements and Specifications of System

3.1 Overview

In this section, we will analyze how the workflow is composed, what hardware is selected, how the necessary software is developed, and finally, how the integration occurred. Generally, a medical-grade multisensory device is used to capture raw ECG data. Using the Bluetooth Low Energy (BLE) protocol, which is designed for short-range communication [29, 91], communication and data acquisition occur between a Raspberry Pi and the medical device. A Python-based interactive web application runs on the Raspberry Pi, allowing users to interact with the multisensory device. Users can select the type of data they want to capture and in the case of ECG, they can also choose to preprocess steps and different feature extraction tools available for analysis. Figure 3.1 presents the overall pipeline on which this thesis is based and will be analyzed in detail in the next sections.

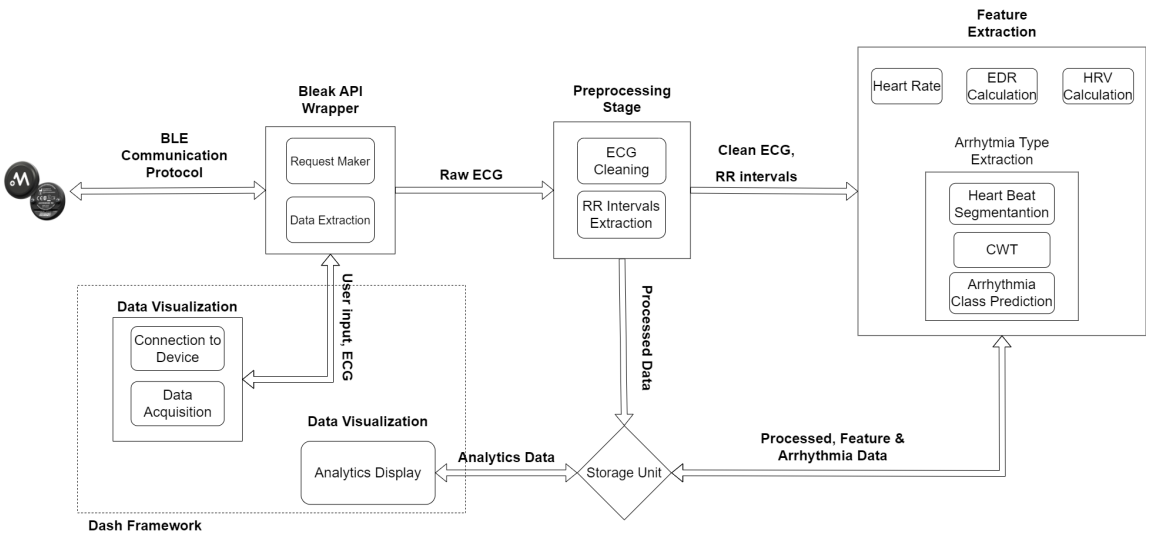

FIGURE 3.1: The overall pipeline of the proposed application.

3.2 Hardware Interface and Embedded Systems

An embedded system combines computer hardware and software designed for a specific function within larger machines or products. Built to be compact, energy-efficient, and often operate in real-time, they are used almost every day by almost everyone. Embedded systems are found in smartphones, smart home devices, automotive systems, and in our case, medical equipment for monitoring vital signs. In our scenario, the embedded systems used are a Raspberry Pi, as the embedded microprocessor unit and the Movesense medical device as the data capturing device.

3.2.1 Microprocessor

As previously mentioned, the Raspberry Pi 4 (figure 4.15) or Pi 5 [22] is the selected microprocessor. Both are compact, affordable and offer strong performance, making them popular choices in many applications. The Raspberry Pi 4 comes with a maximum of 8GB RAM, a quad-core ARM Cortex-A72 processor, support for two 4K displays, and various connectivity choices such as USB 3.0, Gigabit Ethernet and BLE. The Raspberry Pi 5 enhances its hardware, processing speeds, and graphics capabilities for increased performance.

The portability of the Raspberry Pi makes it a perfect fit for our system, enabling seamless integration into different setups and environments, such as portable medical devices. Its ability to consume low power results in extended battery life, allowing for uninterrupted use in mobile and remote healthcare settings. The strong CPUs in the Raspberry Pi 4 and 5 can manage demanding tasks, allowing for real-time processing of intricate medical data. Furthermore, its wide range of connectivity features allows for easy integration with various sensors and devices, like the Movesense medical device, to ensure effective data collection and analysis. The Raspberry Pi benefits from strong community support and detailed documentation, aiding in quick development and problem-solving for our medical monitoring system, ensuring a dependable and efficient solution.

3.2.2 Sensing Device

Movesense Medical [56] (figure 4.14) is used as a sensing device. Classified as Class IIa (MDR [68]) medical device, it is designed for medical use, offering high-quality ECG, heart rate, and movement data for examination. The device comes with a one-channel ECG sensor for measuring heart rate and R-R intervals, as well as a 9-axis motion sensor that includes a 3-axis accelerometer, gyroscope, and magnetometer. It enables customizable sampling frequencies and includes built-in memory for data logging. BLE allows for wireless data transfer and firmware upgrades, along with software utilities for creating customized applications that operate on the sensor. Designed for use in medical, health, and sports settings, this device is both water-resistant (IP68) and shock-proof. It runs on a user-replaceable coin cell battery,

specifically the CR2025 type, and offers software choices to maximize battery duration. The tool is versatile and trustworthy for thorough physiological monitoring, being light at 9.4 grams (0.33 ounces), measuring 36.6 mm (1.44 inches) in diameter, and having a body thickness of 8 mm (0.32 inches).

At the cross-sectional validation study of Rogers et al. [71], the Movesense device suggested as a viable alternative for HRV monitoring. They compared RR intervals and HRV index properties at incremental exercise and at resting states before and after the exercise, from ECG data captured by a conventional 12-channel ECG device and the combination of the movesense medical device attached to the movecese chest strap. The findings showed high agreement between the chest strap sensor and the reference ECG in terms of various HRV measurements and RR interval calculations, with small differences but with excellent correlation during exercise in a time domain metric (mean of RRI) and on a non-linear metric (DFA a1). Overall, the modified lead II recordings from the movesense device are sufficient for capturing accurate ECG data and serve as a reliable tool for HRV computations and feature extraction in both laboratory and remote field applications.

3.3 Software Interface

3.3.1 Communication With The Sensor

To communicate with the BLE device, a Python-based wrapper application programming interface (API) was constructed to connect send requests and save the captured data. The base API is the Bleak one [7] and is an acronym for Bluetooth Low Energy platform Agnostic Klient. It is a GATT client software, capable of connecting to BLE devices acting as GATT servers. It is designed to provide an asynchronous, cross-platform Python API to connect and communicate with e.g. sensors. From the multisensory device view, at the table 3.1, the available data types that can be requested are listed, their code name for use in the wrapper, and the available sampling rates that they support.

GATT is the generic attribute profile and dictates how two BLE devices communicate data through services and characteristics. The diagram 3.2 demonstrates how data is exchanged between a peripheral (GATT Server) and a central device (GATT Client), with the primary device initiating all transactions.

The module that was created to hold the connection and the overall communication consists of a class, named *BLEClient*, and its main methods are listed below.

- *BLEClient.set_device_address(device address)*
  Check if the given address is valid and set it to the client.

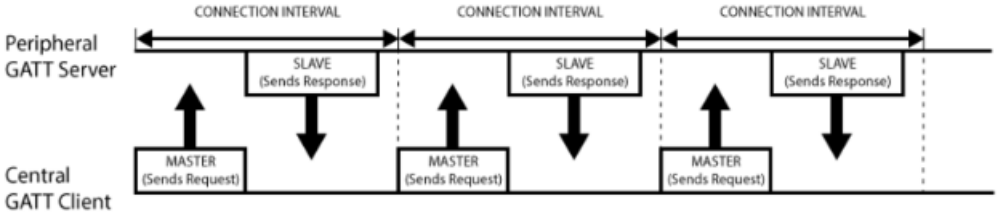

FIGURE 3.2: Server-client data exchange protocol using GATT.

TABLE 3.1: Available data types and sampling rates that can get requested from the Movesense medical device

	Data Type									
	ECG	*HR*	*ACC*	*MAGN*	*GYRO*	*ACC+GYRO*	*ACC+MAGN*	*ACC+GYRO+MAGN*	*TEMP*	*STOP*
Format	"ecg"	"hr"	"acc"	"magn"	"gyro"	"imu6"	"imu6m"	"imu9"	"temp"	"stop"
Rates	X_1		X_2	X_2	X_2	X_2	X_2	X_2		
$\mathbf{X_1}$	13, 26, 52, 104, 208, 416, 833, 1666									
$\mathbf{X_2}$	125, 128, 200, 250, 256, 500, 512									

- *BLEClient.set_client()*
  Set up the Bleak Client object to the class.
- *BLEClient.connect()*
  Connect to the device with the stored mac address.
- *BLEClient.disconnect()*
  Disconnect from the specified device and reset class parameters.
- *BLEClient.write_characteristic(request type, sampling rate, response)*
  Perform a write operation on the specified characteristic of the connected device. Depending on the response, can wait for data after the request is made. Validates the given request type and rate and sets the case of the request for the remote device.
- *BLEClient.start_notify()*
  Activate notifications from the remote device.
- *BLEClient.stop_notify()*
  Deactivate notifications from the remote device.
- *BLEClient.queue.get()*
  Pop out the first element of the class's queue.

3.3.2 Graphical User Interface

Knowing how to communicate with the Movesense device, the user has to interact with the above methods as well as choose how to process the received data. The Dash framework was selected to help with the creation of the graphical user interfaces (GUI). Dash framework [36], built on top of Flask, Plotly and React, produces applications providing a graphical interface for Python models, greatly broadening the capabilities of a conventional "dashboard". Dash plots, graphs, and other visual elements can be easily integrated to create interactive dashboards. The framework supports various visualization libraries like plotly, making it ideal for dynamic data presentation and real-time data analysis. Dash applications are highly customizable, allowing data scientists to focus on delivering insights and visual narratives that can be easily shared and accessed through a web browser.

In our case, two dashboard apps were created, one to give the user different choices to interact with the sensor and one that displayed the different analytics produced by the captured data of the first one. The functionality of each app is listed below.

- Data Acquisition and Processing.
  The user can scan for movesense devices with this app and connect to one. Then, they can select the data types they want to request, set the sampling rate if needed, and make the request. Once the request is made, the notification and recording processes can be activated and a small window displaying the captured data is shown to the user. At the end of the data-capturing process, the processing stage occurs.

  Currently, only ECG data can be displayed and processed at various rates. The user has the option to clean the raw data using one of the cleaning methods discussed in the subsections of chapter 2 or keep the data as it is if the signal-to-noise ratio is satisfactory. Additionally, they can choose a peak detection algorithm to extract the R peak locations from the recorded signal, utilizing one of the algorithms described in the previous chapter as well as, an EDR algorithm to estimate respiration using ECG morphology and features from the previous steps. Finally, the user can verify that the recorded ECG data will pass through a CNN model to detect different arrhythmias types.

- Analytics display.
  In this feature, the user can select one of the recordings stored in the system and display its detailed information. Currently, the user can view several key metrics:

  – *Heart Rate Plot*.
    This shows the heart rate over the capturing time, calculated in beats per

minute (BPM). It provides a clear visualization of heart rate fluctuations during the recording period.

– *Distribution of RR Intervals*.
This plot shows the RR intervals over the entire recording. When the heart rate increases, the RR interval distribution will move towards the left, showing shorter intervals and to the right if the heart rate decreases, showing longer intervals.

– *Respiration Rate Plot*.
This shows the respiration rate over time, calculated in breaths per minute. This helps in displaying the breathing patterns throughout the recording.

Additionally, if any arrhythmias are detected, the entire recorded ECG will be displayed with the types of arrhythmias highlighted over the recording. This allows the user to easily identify abnormal heart rhythms, their type and their occurrences during the recording period. The final information the user can acquire is a table holding the information of the HRV metrics of the desired recording.

3.3.3 Arrhythmia Detection Module

Overview

In this sub-section, an automatic ECG classification method based on CWT and CNN is analyzed. A CNN architecture and preprocessing method are proposed, based on the work of Wang et al. [89], to build an arrhythmia classification system. As shown in figure image 3.3, at the beginning, the dataset used for the training and validation will be analyzed as well as the proposed preprocessing steps needed to extract the features of R peaks data and coefficient matrixes of each heartbeat . Then, the architecture and the training methods are discussed.

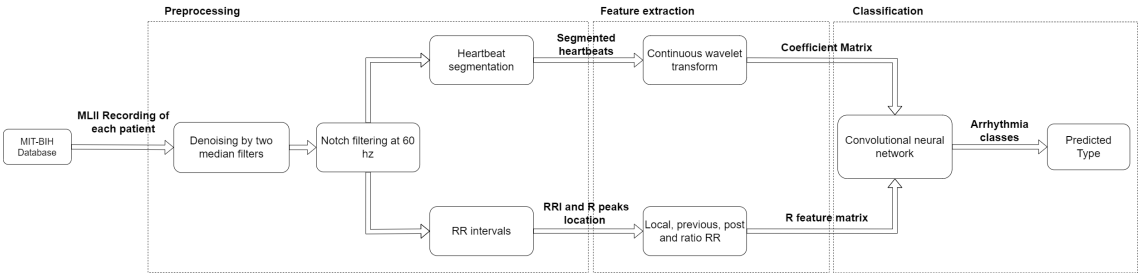

FIGURE 3.3: The overall pipeline of the arrhythmia detection module using CNN.

Dataset

The US-based MIT-BIH arrhythmia database [55] was used as the data source for the training and validation of the network. The database contains 48 recordings, each containing two 30-min ECG lead signals (denoted lead A and B). As described at [14], in 45 recordings, lead A consist of three recordings of lead type V5 and the others as modified-lead II. Lead B is lead V1 for 40 recordings and is either V2, V4, V5, or lead II for the others. Twenty-three of them are intended to serve as a representative sample of routine clinical recordings and 25 recordings contain complex ventricular, junctional, and supraventricular arrhythmias.

For each record, the heartbeats are noted with almost 110 thousand labeled ventricular beats from 15 different heartbeat types, which are noted in table 2.7. We must specify that the set is imbalanced, with over 75 thousand normal heartbeat classes, and just two supraventricular premature beats. Under the AAMI guidelines, four recordings with paced beats were deleted. The rest of the recordings were split into two sets, each consisting of ECG data from 22 recordings with a similar ratio of beat types. Both sets, named DS1 and DS2, consist of around 50 thousand heartbeats and include a combination of regular and intricate arrhythmia recordings. At table 3.2 we can see what record, each patient has and at table 3.3 the heartbeats are associated with the extracted beats types and number for each class, superclass and database. The first one is used for the model training and the second is used to evaluate the performance of the method.

TABLE 3.2: DS1 and DS2 from the MIT-BIH arrhythmia database

DS1	101, 106, 108, 109, 112, 114, 115, 116, 118, 119, 122, 124, 201, 203, 205, 207, 208, 209, 215, 220, 223, 230
DS2	100, 103, 105, 111, 113, 117, 121, 123, 200, 202, 210, 212, 213, 214, 219, 221, 222, 228, 231, 232, 233, 234

To resolve the patient paradigm problem, as highlighted in numerous studies [13, 14, 50], heartbeat classification can be divided into two main paradigms: intra-patient (or class-oriented) and inter-patient (or subject-oriented). The intra-patient paradigm allows portions of the same ECG recording to appear in both the training and testing groups, as it divides the dataset based on beat labels. However, because of inter-individual variance, these classifiers' performance frequently deteriorates in clinical practice. Therefore, to create models that consistently function across a range of patients, inter-patient variability must be addressed for each signal.

Preprocessing

Despite the preprocessing that the record received before they uploaded, baseline wanderer and spikes at 60 Hz exist and interface with the signal quality. For the baseline noise removal, the median filtering method followed as described in chapter 2. Then the signal is introduced to the notch filtering technique, also as described in chapter 2 to remove the power line noise. Here we have to note that for this

TABLE 3.3: Heartbeat types (table 2.7) associated with the AAMI and the extracted beats for the MIT-BIH arrhythmia dataset, DS1 and DS2.

	Heartbeat Class	**N**						**SVEB**					**VEB**			**F**	**Q**				
	Heartbeat Type	NOR	LBBB	RBBB	AE	NE	total (#)	AP	aAP	NP	SP	(#)	PVC	VE	(#)	fVN	P	fPN	U	(#)	total
MIT-BIH	N_c	75054	8074	7259	16	229	90632	2544	150	83	2	2779	7129	106	7235	803	7028	982	33	8043	109492
	total %	68.5	7.4	6.6	0.0	0.2	82.8	2.3	0.1	0.1	0.0	2.54	6.5	0.1	6.62	0.7	6.4	0.9	0.0	7.35	100.0
	A_c	40	4	6	1	5	-	27	7	5	1	-	37	2	-	17	4	3	6	-	-
DS1	N_c	38104	3949	3783	16	16	45868	808	100	32	2	942	3682	415	4097	105	0	0	8	8	51020
	total %	74.7	7.7	7.4	0.0	0.0	89.8	1.6	0.2	0.1	0.0	1.85	7.2	0.8	8.03	0.2	0	0.0	0.01	0.01	100.0
	A_c	18	2	3	1	3	-	14	3	3	1	-	17	10	-	1	0	0	3	-	-
DS2	N_c	36444	4125	3476	0	213	44258	1736	50	51	0	1837	3220	388	3608	1	0	0	7	7	49711
	total %	73.3	8.3	7.0	0.0	0.4	89.0	3.5	0.1	0.1	0.0	3.69	6.5	0.8	7.26	0.0	0.0	0.0	0.0	0.01	100.0
	A_c	19	2	3	0	2	-	13	4	2	0	-	16	7	-	1	0	0	2	-	-

study the main frequency components of the ECG is between 0.1 and 50 Hz, so the impact of the notch filter will not impact the quality morphological feature of each heartbeat.

Having the cleaned signal, the segmentation process has occurred, taking into account the R peak location of each heartbeat. Following the work of [89], the annotated R peak location is used as the fiducial point. Fixed-size heartbeats of 200 samples are acquired to segment the ECG by obtaining 90 samples before and 110 samples after the peaks since the most important waves of the heartbeat appeared to be in this range. This duration (0.55 seconds at 360 Hz) is acceptable since morphological characteristics of the P wave, QRS complex and a significant portion of the T wave, are captured within this range. Additionally, many arrhythmias exhibit differences from normal beats within this interval, ensuring that critical features of the heartbeat are preserved.

Having each record segmented, the CWT of each heartbeat is calculated. Four cases were created with each one of the transform heartbeats with one of the mother wavelets noted in chapter 2 (morl, mexh, gaus4 and gaus8). Because the valid information of each ECG is the bandwidth of $0.1 - 50$ Hz, the scales are carefully selected. Because of the nature of each mother wavelet, there is the case that at low scales, the central frequency the wavelet focuses on. is bigger than 0.1, and in some cases of 2.5 Hz (morlet with 100 scales). To resolve this, 256 different scales were selected, to focus on the desired frequency range. After the completion of the transform, matrixes with the coefficients of each scale are created and saved for each heartbeat and each record.

A visual example of scaled scaleograms of ECG at logarithmic scale, with abnormal heartbeats, and for each wavelet, can be viewed in figure 3.4. The section presented is in the presence of noise and for this reason, the information is focused on frequencies other than the ones we are interested in. Figure 3.5, represents the same segment after the noise removal process, where the magnitude information is mainly 'focus' on the QRS complexes and in figures 3.6 3.7 the single segments of abnormal and normal beats, where their coefficient matrixes will be fed to the CNN model.

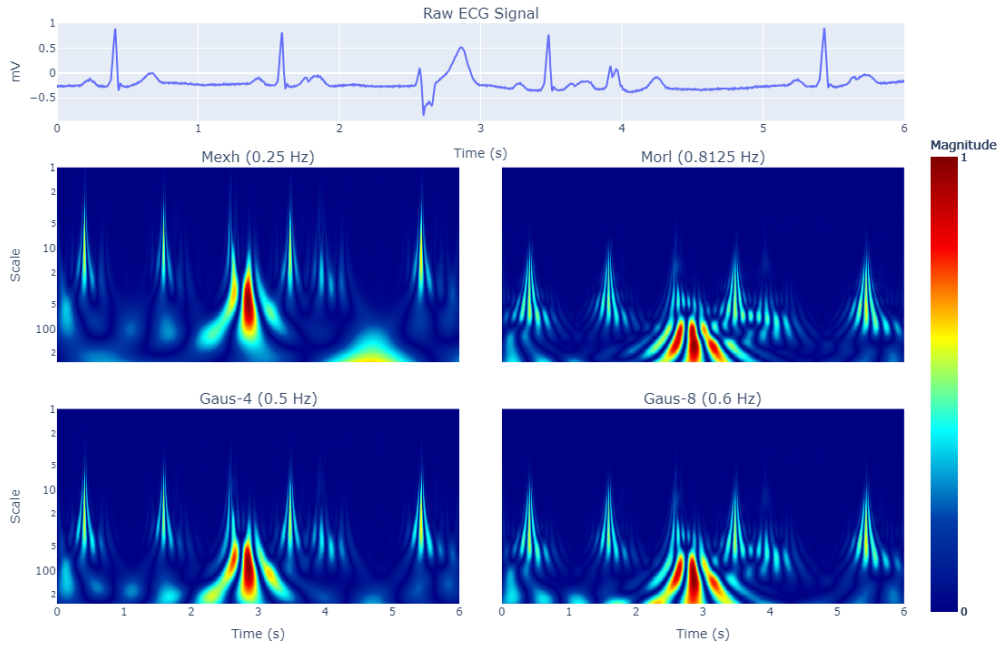

FIGURE 3.4: Scaleograms of abnormal ECG after CWT in the presence of noise.

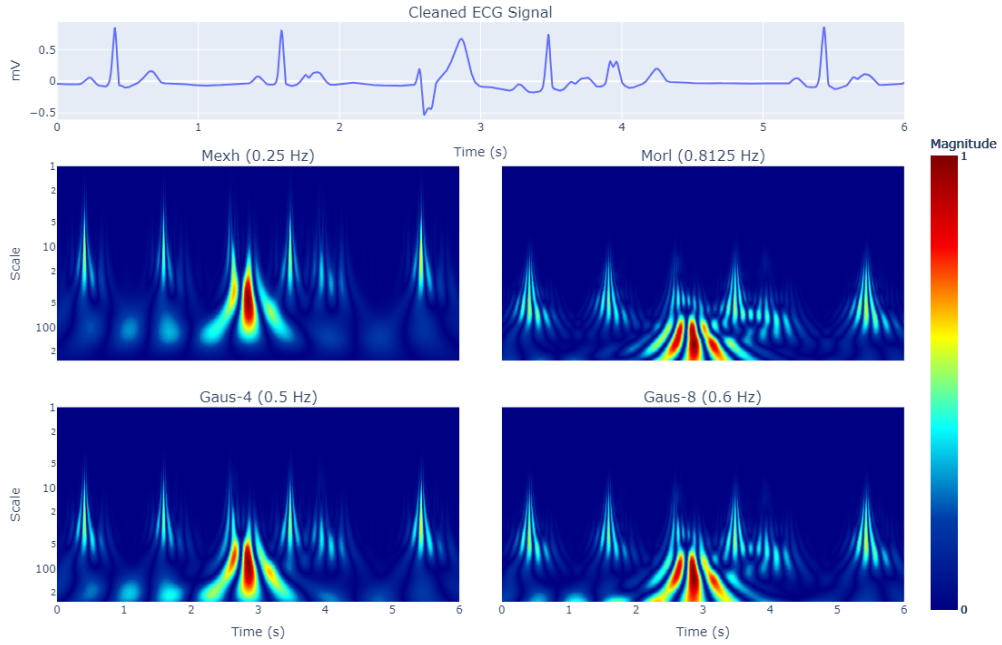

FIGURE 3.5: Scaleograms (log scale) of abnormal ECG after CWT and after noise removal.

Another batch of features that had to be calculated before the training of the model, was metrics of RR intervals for each beat. Following the pipeline figured in image 3.1, the previous RR-interval was the RR-interval between a given heartbeat and its previous one, as the name notes. while the post-interval was the interval between the given heartbeat and the following heartbeat. The ratio RR or the ratio of the

length of one RR interval to the length of the following RR interval gives insight into the relationship between consecutive heartbeats. Finally, the local average RR interval was determined by averaging the valid RR intervals of ten heartbeats surrounding the wanted one.

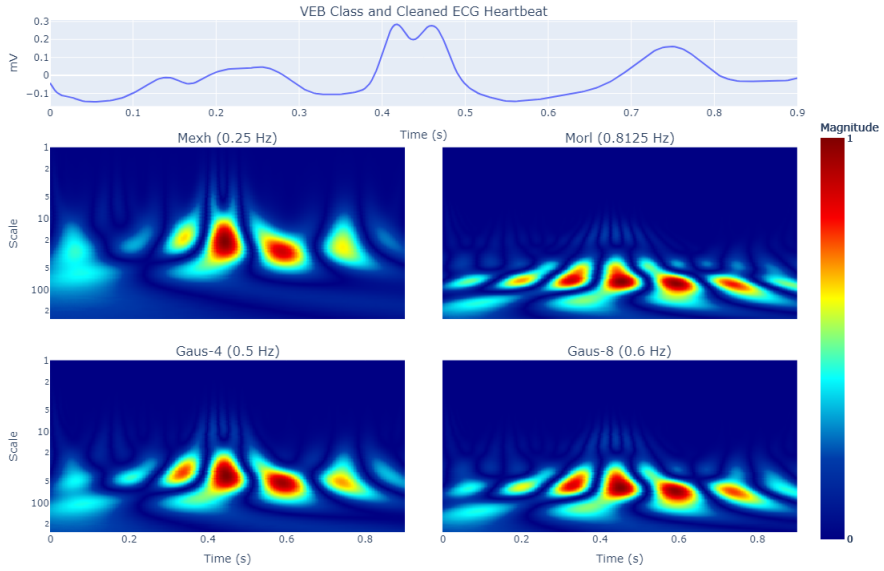

FIGURE 3.6: Scaleograms (log scale) of an abnormal heartbeat after CWT.

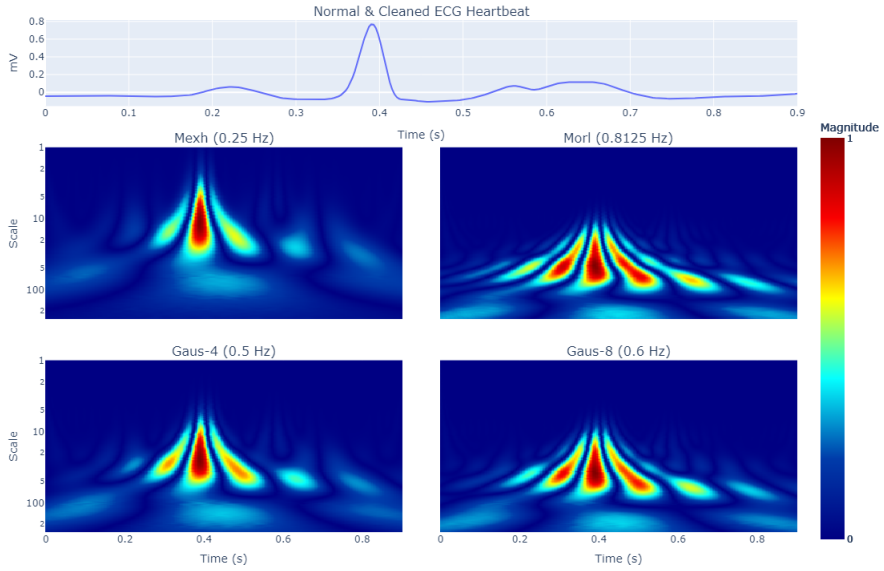

FIGURE 3.7: Scaleograms of an normal heartbeat after CWT.

If focus only on the single heartbeats that are visualized in figures 3.6 and 3.7 their difference is noticed, but the magnitude is scaled concerning the morphological characteristics of each one of them, reducing their separability. To understand better the true big separability they have, figure 3.8 displays the above heartbeats, their coefficients for each scale, and the synced class of each heartbeat to highlight the noted

difference.

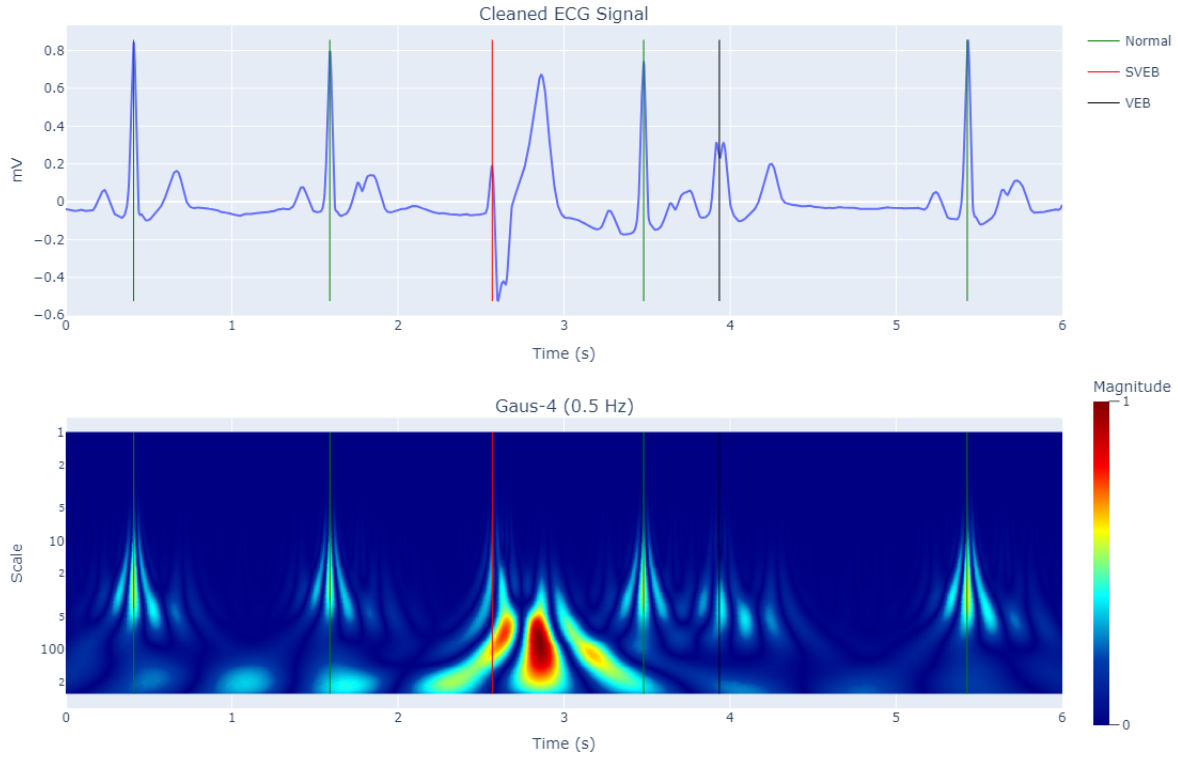

FIGURE 3.8: Scaleograms (log scale) of normal and abnormal (SVEB & VEB) heartbeats after CWT with GAUS4.

CNN Model and Training Setting

The model architecture used for feature extraction and the fully connected layers at the bottom as the MLP is displayed in table 3.4.

During the training process of the CNN with the MLP classifier, cross entropy is taken as the loss function, and Adam is used as the optimizer due to the ability to speed up the training process. The training process and the model creation are run on PyTorch [60] and trained on the NVIDIA GeForce RTX 4060 GPU. The starting learning rate is set at 0.001 and is decreased by 10% every 5 epochs. The model's batch size is 1024 with a maximum of 30 epochs. To furthermore speed up the training process, the fully connected weights of the convolutional layers are initialized with the He et al. initialization method [32] (also known as Kaiming normalization).

Except for the MPL, an SVM classifier was used to make predictions. The input of the SVM is the features extracted from the CNN in table 3.4. The kernel used to create decision boundaries is the radial basis function (RBF) kernel [85], also known as the Gaussian kernel. It measures the similarity between two data points in infinite dimensions and then approaches classification by majority vote. and it is the default kernel for SVMs in the scikit-learn python package [63], which is used in this thesis.

TABLE 3.4: CNN architecture for feature extraction and the MLP for prediction making and their parameters,

Layer Type	**Kernel Size**	**Filter**	**Padding**	**Stride**	**Output Shape**	**Parameters**
Input Of Coefficients	-	-	-	-	$100 \times 100 \times 1$	-
Conv2d	7×7	16	0	1	$94 \times 94 \times 16$	784
Batch Normalization	-	-	-	-	$94 \times 94 \times 16$	64
ReLU	-	-	-	-	$94 \times 94 \times 16$	-
Max Pooling	5×5	-	0	5	$18 \times 18 \times 16$	-
Conv2d	3×3	32	0	1	$16 \times 16 \times 32$	4608
Batch Normalization	-	-	-	-	$16 \times 16 \times 32$	128
ReLU	-	-	-	-	$16 \times 16 \times 32$	-
Max Pooling	3×3	-	0	3	$5 \times 5 \times 32$	-
Conv2d	3×3	64	0	1	$3 \times 3 \times 64$	18432
Batch Normalization	-	-	-	-	$3 \times 3 \times 64$	256
ReLU	-	-	-	-	$3 \times 3 \times 64$	-
Final Max Pooling	3×3	-	-	-	$1 \times 1 \times 64$	-
Flatten	-	-	-	-	64	-
Input of RR Metrics	-	-	-	-	4	-
Concatenate	-	-	-	-	68	-
Dense	-	-	-	-	32	2208
Dense	-	-	-	-	4	132

Chapter 4

Results

4.1 CNN metrics

To start the training process, two variations of the datasets were created. The first one consists of the DS1 and DS2 with only the baseline noise removed, and the other with both baseline and power line noises removed. Then, each record was segmented into individual heartbeats, with the removal of paced and unknown beats, as well as the patient variation of each record. For each heartbeat, RR metrics were calculated and later the coefficient matrixes in order to fed into the network. The coefficient was the result of the CWT of each heartbeat with one of the mother wavelets at 256 scales. Every one of the four recommended wavelets was tested.

The evaluation metrics, described in chapter 3, for this multi class classification problem, are delayed at table 4.1. Due to the imbalanced dataset, the F1 score is taken as the leading performance metric, to compare the different approaches.

Looking at each class separately, the best metrics occurred at the below combinations:

- **N** class:
  The use of *median and notch* filtering at each record to create DS1 and DS2 and the *gaus4* mother wavelet to create the coefficients, achieved the highlighted F1 score of 98.65%, surpassing other combinations of the same class with a maximum percentage difference of 0.56%.

- **SVEB** class:
  Also, the use of *median and notch* filtering at each record to create DS1 and DS2 and the *gaus4* mother wavelet, achieved the maximum F1 score of 80.75%, and a difference of 24.35% from the other.

- **VEB** class:
  The use of *median* filtering at each record and the *morl* wavelet, achieved the maximum F1 score of 95.89%, and a difference of 2.36% from the other. It mast highlighted that the combination of *median and notch* filtering and *gaus4* wavelet variation achieved 93.9% f1 score, a difference of 2.08%

- **Q** class:
  The Q class consists mostly of a combination of ventricular and regular beats that closely resemble the normal heartbeat, posing a challenge for the classifier to differentiate them. The CNN mentioned can extract distinctive features on its own, but the dataset has a restricted number of classes. Overall, the maximum f1 score achieved is 0.5% with the highest metrics of precision and recall of 10% and 0.26% (very low) respectively. The variation that occurred is again with the use of *median and notch* filters at the preprocessing step and the *gaus4* at the feature extraction set.

TABLE 4.1: Evaluation metrics of each class after CNN training. Metrics are exported for each wavelet and each preprocessing method. M stands for the datasets that filtered only with (M)edian filter and M-N for them that filtered with (M)edian and (N)otch filters

		MEXH		MORL		GAUS4		GAUS8	
Class	**Metric (%)**	M	M-N	M	M-N	M	M-N	M	M-N
N	Precision	97.68	96.64	96.87	97.02	97.81	98.22	97.76	97.54
	Recall	99.20	99.62	99.34	99.30	99.37	99.08	99.27	99.42
	F1 score	98.43	98.11	98.09	98.15	98.59	**98.65**	98.51	98.47
SVEB	Precision	84.02	89.10	75.57	77.59	84.22	82.90	83.53	88.49
	Recall	68.74	41.83	44.99	53.00	62.80	78.70	64.11	68.25
	F1 score	75.61	56.93	56.40	62.98	71.95	**80.75**	72.54	77.06
VEB	Precision	94.43	94.61	96.16	96.52	94.69	92.70	92.40	95.37
	Recall	94.22	93.79	95.62	93.94	96.86	95.12	95.99	92.79
	F1 score	94.32	94.20	**95.89**	95.21	95.76	93.90	94.16	94.06
Q	Precision	0.0	0.0	0.0	0.0	1.33	10.00	0.0	2.22
	Recall	0.0	0.0	0.0	0.0	0.26	0.26	0.0	0.26
	F1 score	0.0	0.0	0.0	0.0	0.43	**0.5**	0.0	0.46

In table 4.2, we can also observe some other average metrics of the process. The macro average F1 score on the processed set with the median-notch filter and gaus4 wavelet transform shows the highest metric at 68.45%. In this same case, the macro overall metrics of precision and recall also demonstrate higher performance, with precision at 70.96% and an average difference of $\pm$2.04% with other cases and recall at 68.29% and an average difference of $\pm$5.17%, respectively. This average metric,

as shown at chapter 2, calculates each class's performance metric and then takes the arithmetic mean across all classes giving equal weight to each class, regardless of the number of instances. Due to the large amount of N classes and the small amount of Q this metric is not approximated by the individual scores discussed earlier. For that reason, if we note the weighted metrics, which take into account the balance of classes, each class is based on its representation in the dataset. Also, here the median-notch combination and the gaus4 wavelet give the best results with a metric of 96.91%.

TABLE 4.2: Average evaluation metrics of each wavelet-dataset combination after CNN training.

		MEXH		MORL		GAUS4		GAUS8	
	Metric(%)	M	M-N	M	M-N	M	M-N	M	M-N
Macro	Precision	69.03	70.09	67.15	67.78	69.51	70.96	68.43	70.91
	Recall	65.54	58.81	59.99	61.56	64.82	68.29	64.84	65.18
	F1 score	67.09	62.31	62.59	64.08	66.68	**68.45**	66.30	67.51
Weighted	Precision	96.2	95.47	95.28	95.51	96.35	96.61	96.12	96.32
	Recall	96.98	96.33	96.31	96.47	97.08	97.30	96.98	97.06
	F1 score	96.55	95.57	95.64	95.89	96.65	**96.91**	96.50	96.63

4.2 SVM Metrics

The model utilizing the SVM classifier produced lower metrics for all classes except for the Q class. In the Q class, the F1 score was 0.75% when using median-notch filtering combined with the Mexican hat wavelet for feature extraction. For the other classes, the maximum metrics for the N and VEB classes were slightly lower in comparison to the metrics achieved by the MLP classifier. However, the SVEB class metrics were notably smaller in all cases, indicating a reduction in performance for this particular class when using the SVM classifier. This suggests that while the SVM model may have certain strengths, particularly for the Q class, it generally underperforms compared to MPL, especially for the SVEB class.

4.3 Selected Model

Based on the results, the selected approach for this study integrates both median and notch filters during preprocessing, in conjunction with the Gaussian wavelet with four derivatives for feature extraction. The VEB class demonstrates notable

performance, not only due to its generally high metrics but also because of its minimal deviation from the maximum values. Table 4.3 presents the confusion matrix for the training and evaluation processes, with all values normalized. In this table, the maximum values are highlighted in bold and positioned along the diagonal of the matrix, except for the Q class, which is characterized by having the fewest elements, as previously described.

TABLE 4.3: Normalized confusion matrix of selected model.

True Label	Predicted Label			
	N	**SVEB**	**VEB**	**Q**
N	**0.991**	0.006	0.003	0.0
SVEB	0.169	**0.787**	0.042	0.008
VEB	0.039	0.01	**0.951**	0.001
Q	0.94	0.0	0.056	0.002

4.4 R Peak Algorithm Comparison

In this study, three ECG cleaning and four R peak detection algorithms were selected. The extension of the work proposed by Porr & Howell [66] and the one made by authors of the Neurokit toolbox, made for this thesis and compares the different peak detection algorithms that use the noted cleaning methods. Three large and labeled ECG databases are taken as references (MIT-BIH Arrhythmia Database [55], MIT-Normal Sinus Rhythm Database [28] and Glasgow University Database [34]). Their recordings are processed and R locations are extracted, using different R peak detection algorithms, for benchmark and validation purposes. First, the amount of errors in peak detection is calculated by computing the absolute distance from the original "true" R-peaks location. As such, the closer to zero, the better the accuracy.

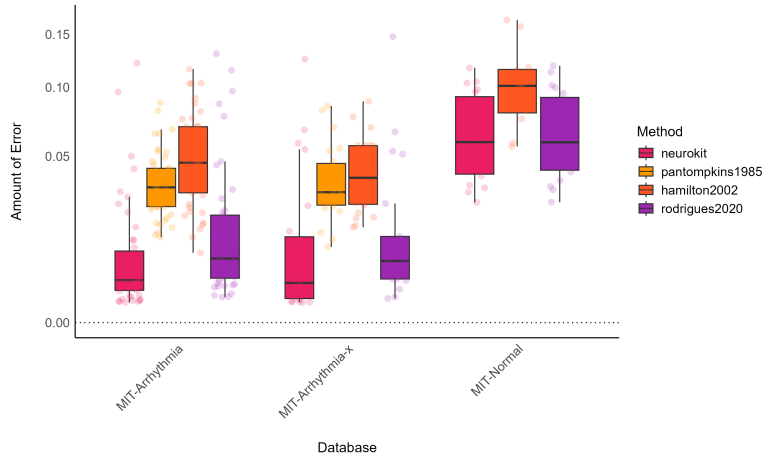

FIGURE 4.1: Accuracy of R-peak detection algorithms across different databases.

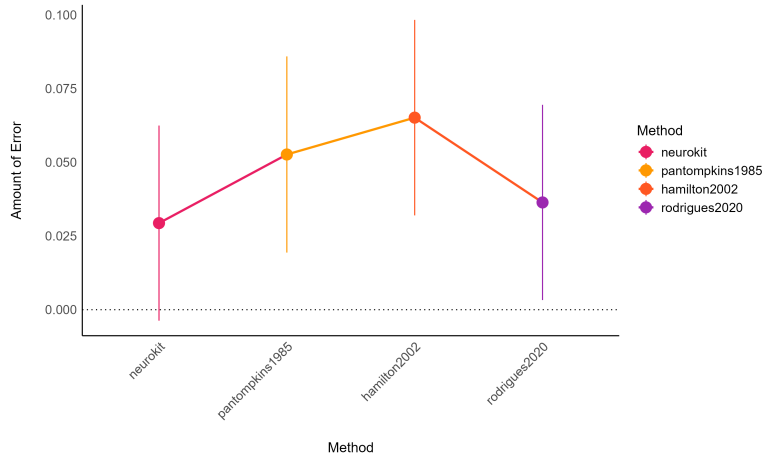

FIGURE 4.2: Statistical view of 4.1.

Figure 4.1 shows the descriptive statistics of the results, and figure 4.2 holds the view

of its statistical model. The result suggests that Neurokit's and then, Rodrigues's implementations are the least prone to errors. Also, we have to note that the Pan and Tompkins algorithm didn't produce results for the MIT Normal database due to the way it works (need for a certain number of peaks at least to work).In terms of computation time needed, figures 4.3 and 4.4 identify that Neurokit's and Pan and Tompkins's implementation algorithms are faster compared with Rodrigues and Hamilton's.

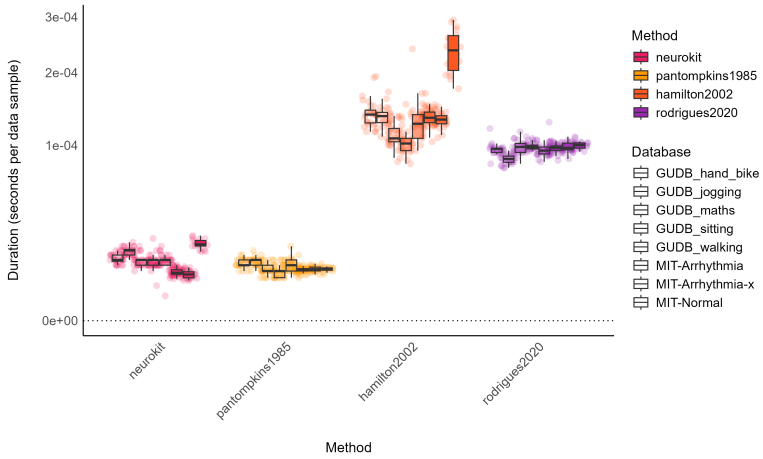

FIGURE 4.3: Time needed for R-peak detection of each algorithm and for each database.

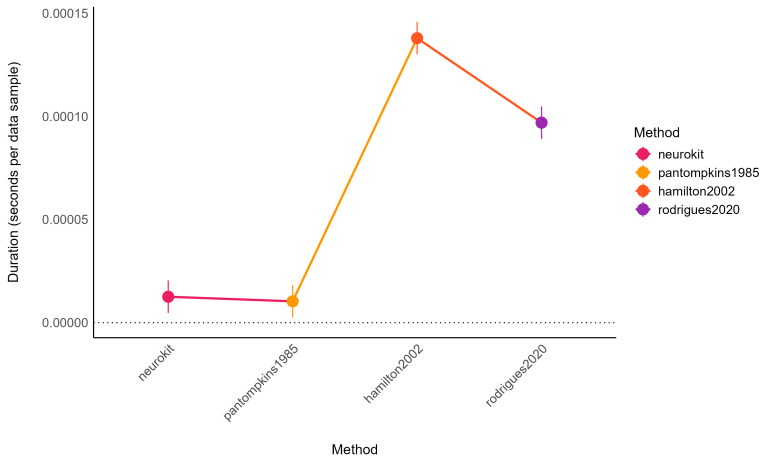

FIGURE 4.4: Statistical view of 4.3.

4.5 Applications

In this section, we will discuss the two applications that host the GUIs and the communication methods between the user and the Raspberry Pi processes running in the background.

- Capture and Processing App.

  The overall initial state of the app is shown in the figure 4.5.

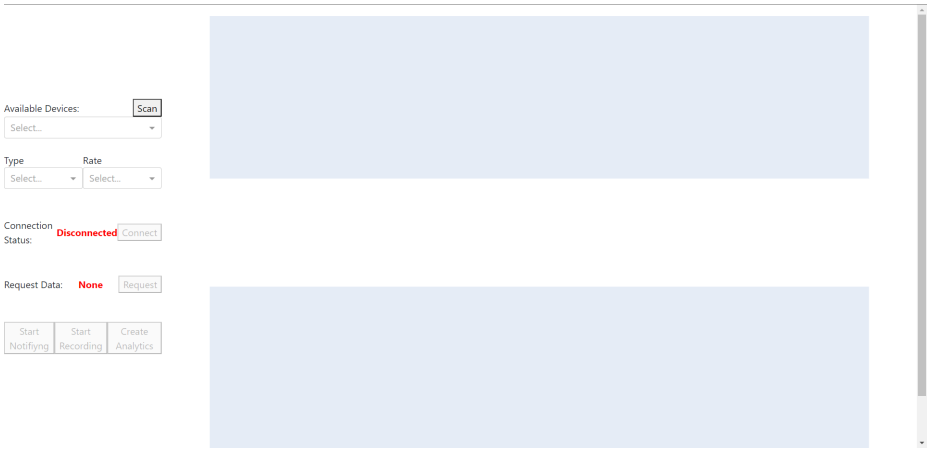

FIGURE 4.5: The initial state of the capture and processing app.

From left to right, the user can view and interact with the dashboard responsible for communicating with the Movesense device and two placeholders that showcase the captured data. Figure 4.6 shows an example of what the user will see on the dashboard after scanning for Movesense devices, connecting to one of them, selecting the desired data type and sampling rate, and making the request.

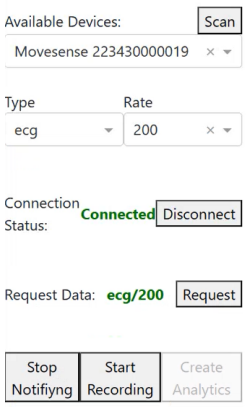

FIGURE 4.6: An example showcasing the dashboard after connecting and requesting to the sensor.

The next figure (4.7), displays a snapshot of it while data are retrieved from the multisensory device.

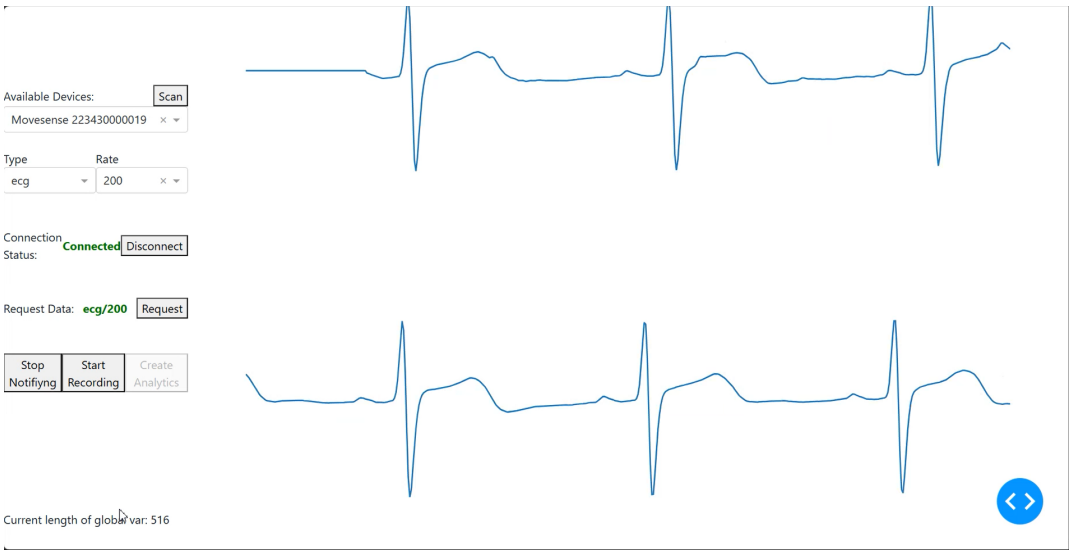

FIGURE 4.7: A visual example of data capturing using the suggested app.

While capturing data, the user can select the *Start Recording* button, to save the received information. Later, and while the data are stored, the *Create Analytics* button can get selected and result in a pop-up modal window that holds all the information and choices the user has, to process the received data, and save the results as shown at image 4.13.

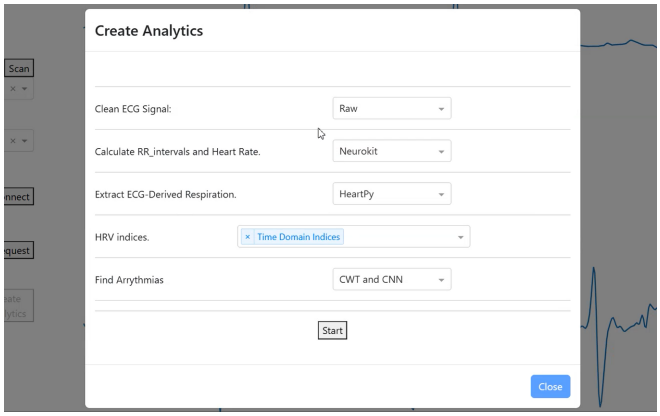

FIGURE 4.8: A visual example of the process choices the user has for the captured ECG signal.

After following the previous steps, the user can move on to the next implementation, to display the data.

- Analytics Display App.

  Interacting with the analytics display dashboard, the user will see the initial state of the page as shown in image 4.9.

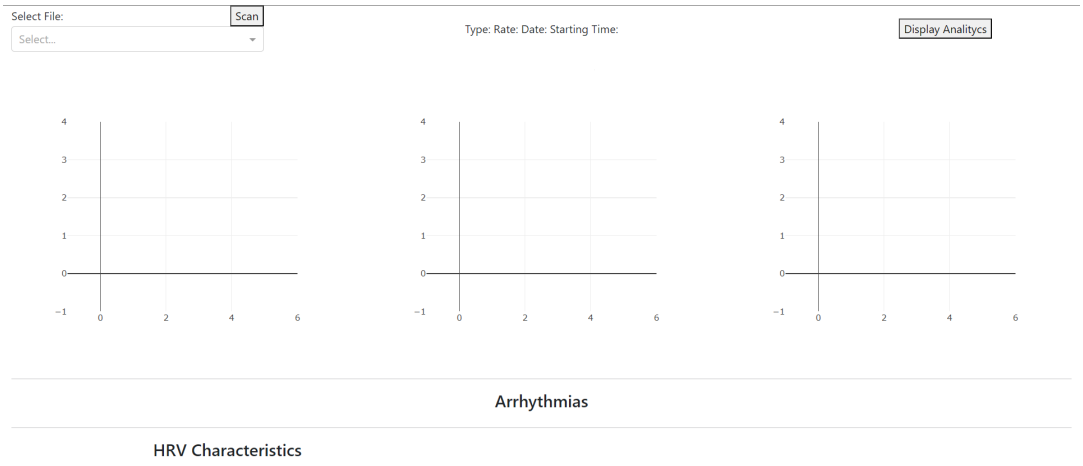

FIGURE 4.9: [The initial state of the analytics display app.

The user can scan for saved data and select one for display. The filename format follows the structure *data-type_captured-date_captured-time_sampling-rate*. Upon selecting the display option, from top to bottom, the user can interact with the heart rate plot, the distribution plot holding of RR intervals and an estimation of breath rate calculated from the recorded ECG features. In the middle section, the arrhythmias mini page displays recorded ECG and arrhythmia types, if they exist. Finally, a matrix containing the chosen HRV metrics calculations is provided. The images 4.10, 4.11 and 4.12, give an example of the above and image 4.11 is a visual example of the interacted plot, displaying arrhythmias of VEB types, on an ECG captured from a user diagnosed with atrial fibrillation

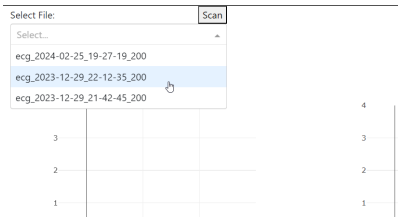

FIGURE 4.10: The scanning result of the Display App.

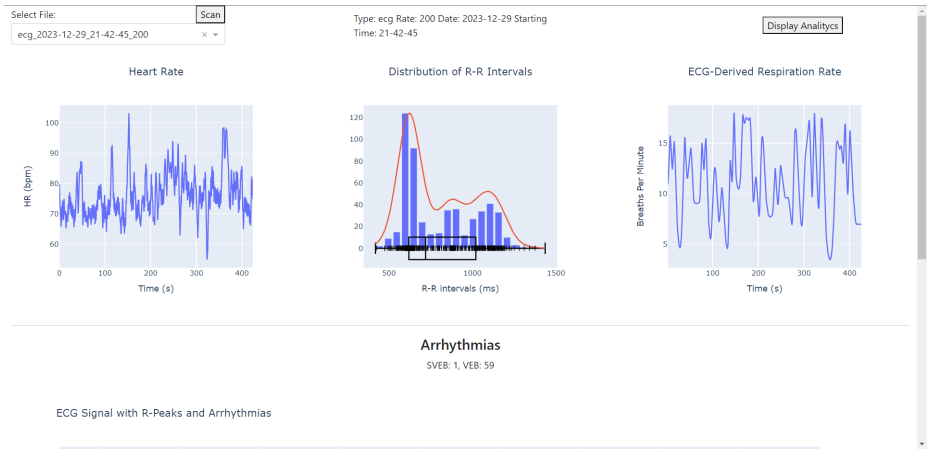

FIGURE 4.11: Snapshot of the analytics display apart I.

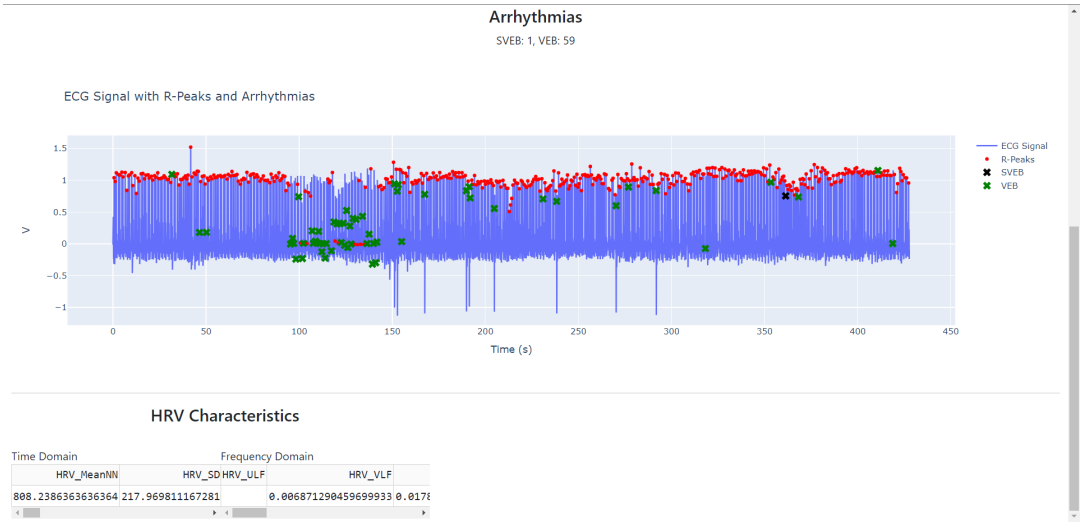

FIGURE 4.12: Snapshot of the analytics display app, part II.

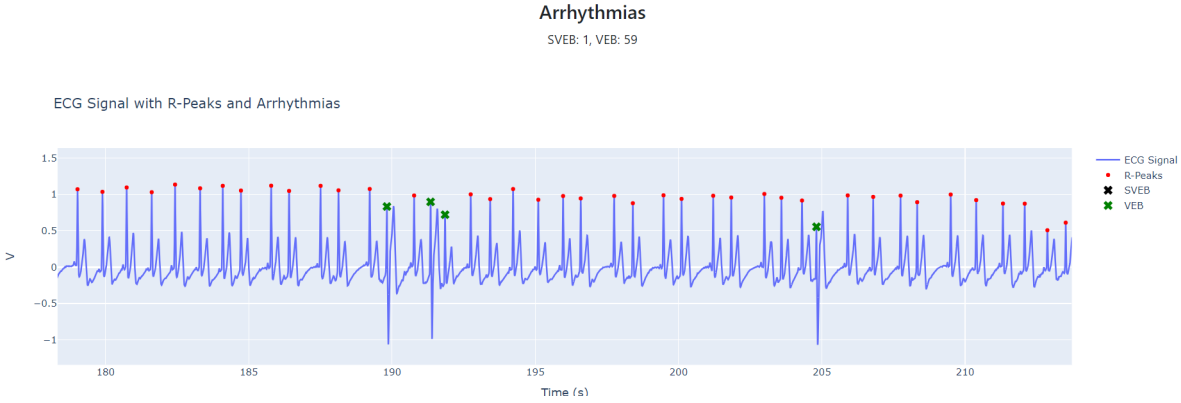

FIGURE 4.13: An example of an ECG sample containing predicted arrhythmia types.

4.6 Hardware

The hardware parts used for the proposed system are listed and displayed below.

- Movesence Device and Chest Belt.

  The multi-sersoring device used for capturing medical grade ECG of modified lead II type (attached to the chest belt)

FIGURE 4.14: The multisensory device Movesense Medical is attached to an electrode (bottom) and the chest belt used (top).

- Raspberry Pi 4 Model B.

  The microprocessor used, stands as the computation unit, allowing the user to communicate with the sensor and view the stored analytics.

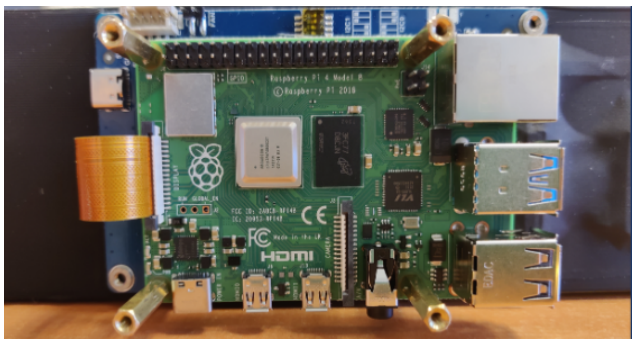

FIGURE 4.15: The Raspberry device, hosting the hole system, attached to the Waveshare monitor driver.

- Whaveshare Monitor & Power Suply Unit.

  The power unit of the system and the touch monitor allowing the user to interact with the microprocessor.

FIGURE 4.16: The front view of the monitor and a power unit.

- 3D Case.

  The 3D case used, to house all the system components.

FIGURE 4.17: The 3d case hosting the raspberry unit attached to the monitor.

Chapter 5

Discussion

In this work, a Raspberry Pi was employed alongside a Movesense medical device to create a system for medical signal monitoring signals and processing. The project involved the development of two cross-platform APIs, one for communication with users, and a graphical user interface one to facilitate user interaction with the device. Additionally, code was implemented for preprocessing tasks, including feature extraction from captured ECG signals and arrhythmia detection.

The arrhythmia detection model utilized a CNN trained on the MIT-BIH Arrhythmia dataset. This model achieved impressive metrics, with an F1 score of 80.75% for the Supraventricular Ectopic Beat class and 93.9% for the Ventricular Ectopic Beat class. The preprocessing of the dataset demonstrated the impact of using a different wavelet than the widely used Mexican Hat, as well as the combined effect of a notch filter alongside a median filter. These preprocessing techniques produced better results compared to the ones found in the literature, which typically use MEXH and only median filters. These findings highlight the effectiveness of the proposed system in accurately detecting and classifying arrhythmias, thereby contributing to advancements in medical diagnostics for supporting the monitoring of cardiovascular problems, which are the leading cause of death globally. Furthermore, the impact and the accuracy of the selected model on medical-grade ECGs, which include records from healthy subjects and records from subjects with atrial fibrillation (post-surgery), were validated by the healthcare staff of ΠΑ.Γ.Ν.Η. hospital (expert title: 'Nurse Specialized in Cardiovascular Diseases').

Despite significant progress in utilizing the API for sensor communication, it is essential to acknowledge its limitations. The current API implementation exhibits occasional bugs that can affect data reliability. For example, inconsistencies in data transmission may necessitate a hardware reset of the multisensory device to restore proper functionality. To address these issues, one potential improvement strategy involves enhancing the asynchronous logic governing sensor communication. Additionally, capturing multiple data types consecutively with minimal intervals between requests could help mitigate data loss by filling gaps through interpolation or

other suitable methods. These advancements aim to enhance overall data integrity and reliability in sensor-based applications.

Regarding the graphical user interface, although it provides essential features, it has certain limitations. The current GUI includes only the fundamental elements for sensor communication and data display. Potential improvements could involve expanding its functionality by integrating additional interfaces to support a broader range of data types, such as accelerometer, gyroscope, and heart rate data. This enhancement would enable users to visualize and analyze a more comprehensive array of data within the same analytical application interface.

For the suggested EDR algorithms, which extract respiratory information from ECG signals similar to R peak detection algorithms, validation is critical to ensure their accuracy and reliability across various physiological conditions and practical settings. Furthermore, a thorough examination of the respiratory signal may uncover additional characteristics, enhancing the understanding of a patient's health condition.

As previously mentioned, the inspiration for the arrhythmia detection algorithm was taken from the work of Wang et al. [89]. In their study, they suggest that their classifier achieves an F1 score of 81.37% for the SVEB class and 94.43% for the VEB class, metrics much more improved from similar works, as shown in table 5.1

TABLE 5.1: Classification performance of existing works in SVEB and VEB classes

	SVEB (%)				VEB (%)			
Methods	Precision	Recall	F1 score	Accuracy	Precision	Recall	F1 score	Accuracy
Liu et al. [41]	39.87	33.12	36.18	95.49	75.61	90.2	82.79	97.45
Chen et al. [16]	38.40	29.50	33.36	95.34	85.25	70.85	77.38	97.32
Zhang et al. [95]	35.98	79.06	49.46	93.33	92.75	85.48	88.96	98.63
Ye et al. [93]	52.34	61.02	56.34	96.27	61.45	81.82	70.19	95.52
Garcia et al. [25]	53.00	62.00	57.15	–	59.40	87.30	70.70	–
Wang et al. [89]	89.54	74.56	81.37	98.74	93.25	95.65	94.43	99.27
Wang et al. Reproduction	77.9	73.91	75.85	73.9	91.39	93.69	92.53	93.8
Proposed Strategy	**82.90**	**78.70**	**80.75**	**78.70**	**92.70**	**95.12**	**93.90**	**95.10**

Despite following their suggested architecture and attempting to reproduce the study, it was unable to achieve the results reported in the original work. Specifically, for the SVEB class, the recorded F1 score was 75.85%, which is 7.27% lower than their reported value. Similarly, for the VEB class, the F1 score was 92.53%, almost, 2% lower than theirs. One plausible explanation for these discrepancies could be the differences in hardware and package versions used in the experiments. However, the significant difference in the SVEB class suggests additional factors at play. Notably, during the feature extraction step, the CWT scales (100), compared with the mexh wavelet central frequency (0.252), may omit frequencies in the low frequency

(LF) bandwidths, where much crucial ECG signal information resides. Finally, their training of the algorithm did not utilize cross-validation like k-fold, and the metrics were obtained from a single pass.

For the above reason, a retraining of our studied model was conducted using the technique of k-fold validation. Generally, k-fold cross-validation involves dividing the dataset into k equally sized subsets, or "folds." From this division, unique indexes of training and validation data are derived to train the CNN model. The performance metrics are calculated for each of the k iterations, and the final performance metric is the average of the metrics from all k iterations and can be viewed at tables 5.2 and 5.4. In terms of F1- score the maximum results taken from this method and for each method are displayed below.

- **N** class:
  The use of only *median* filtering at each record and the *gaus4* mother wavelet to create the coefficients, achieved F1 score of $99.5\% \pm 0.01e-16$.
- **SVEB** class:
  The use of *median and notch* filtering and the *morl* mother wavelet, achieved the maximum F1 score of $87.5\% \pm 0.01e-16$.
- **VEB** class:
  The use of *median* filtering and the *gaus8* wavelet, achieved the maximum F1 score of $97.6\% \pm 0$.
- **Q** class:
  Despite the restricted number of data for this class, the maximum f1 score achieved is $81.1\% \pm 1.12e-16$ with the use of *median* filtering at the preprocessing step and the *gaus4* wavelet at the feature extraction set.

Despite the N and VEB classes maintaining high-performance metrics, the Q class exhibited high metrics despite its limited data. This demonstrates that the Q class performed exceptionally well, which is noteworthy given the low number of records available for this class. In contrast with the chosen model, the SVEB and Q classes showed a notable increase in performance metrics compared to the previous models, indicating improvements.

The average metrics, also taken into account (tables 5.3, 5.5) and as shown, every F1 score metric hold a high value. Since both weighted and macro F1 scores are high, it suggests that the model is consistently effective across different classes and not overly biased toward any particular class.

In this study, the entire MIT-BIH database was used, rather than splitting it into subsets like DS1 and DS2. This approach presents a challenge related to the patient paradigm. Specifically, k-fold cross-validation might result in the same patient's heartbeats appearing in both the training and validation sets (although not the same heartbeats). It is crucial to ensure this does not introduce bias. Currently, there

is no in-depth research addressing this issue. One possible solution is to modify the validation set to include records from patients who are not represented in the training set.

Another observation is that the standard deviations for each metric and class are nearly zero, even after numerous runs with varying initial states. This consistency might be due to the CWT coefficients for different heartbeat classes being morphologically distinct and well-separated, which makes classification easier. However, the lack of further investigation into this variability or potential overfitting raises concerns. This consistency in performance metrics might indicate a need for additional analysis to fully understand the implications of these results.

TABLE 5.2: Average of evaluation metrics of each class after CNN training using 5-fold cross-validation technique. Metrics are exported for MEXH and MORL wavelets and each preprocessing method.

		MEXH		MORL	
Class	**Metric**	M	M-N	M	M-N
N	Precision	$99 \pm 1.1e-14\%$	$98.8 \pm 1.1e-14\%$	$99 \pm 0\%$	$99.1 \pm 1.1e-14\%$
	Recall	$99.8\% \pm 1.1e-14$	$99.8 \pm 0\%$	$99.8 \pm 1.1e-14\%$	$99.8 \pm 0\%$
	F1 score	$99.4\% \pm 1.1e-14$	$99.3 \pm 0\%$	$99.4 \pm 0\%$	$99.4 \pm 1.1e-14\%$
SVEB	Precision	$92 \pm 1.1e-14\%$	$94.6 \pm 0\%$	$93.1 \pm 0\%$	$95.3 \pm 0\%$
	Recall	$80.2 \pm 1.1e-14\%$	$76.5 \pm 0\%$	$79.8 \pm 0\%$	$80.9 \pm 0\%$
	F1 score	$85.7 \pm 1.1e-14\%$	$84.6 \pm 0\%$	$86 \pm 1.1e-14\%$	$\mathbf{87.5 \pm 0}\%$
VEB	Precision	$98 \pm 0\%$	$95.6 \pm 1.1e-14\%$	$97.7 \pm 0\%$	$96.5 \pm 0\%$
	Recall	$96 \pm 1.1e-14\%$	$96.4 \pm 1.1e-14\%$	$96.6 \pm 1.1e-14\%$	$96.9 \pm 1.1e-14\%$
	F1 score	$97 \pm 1.1e-14\%$	$96 \pm 1.1e-14\%$	$97.2 \pm 1.1e-14\%$	$96.7 \pm 0\%$
Q	Precision	$89.8 \pm 1.1e-14\%$	$92.5 \pm 0\%$	$89.9 \pm 0\%$	$92.7 \pm 1.1e-14\%$
	Recall	$64.2 \pm 0\%$	$44.9 \pm 0\%$	$59.6 \pm 0\%$	$69.7 \pm 0\%$
	F1 score	$74.9 \pm 0\%$	$60.4 \pm 0\%$	$71.5 \pm 0\%$	$79.6 \pm 0\%$

TABLE 5.3: Average evaluation metrics of MEXH & MORL wavelets after CNN training.

		MEXH		MORL	
Class	**Metric**	M	M-N	M	M-N
Macro	Precision	$94.7 \pm 0\%$	$95.4 \pm 0\%$	$94.9 \pm 0\%$	$95.9 \pm 0\%$
	Recall	$85.1\% \pm 0$	$79.4 \pm 0\%$	$83.9 \pm 1.1e-14\%$	$86.8 \pm 0\%$
	F1 score	$89.2\% \pm 1.1e-14$	$85.1 \pm 1.1e-14\%$	$88.5 \pm 1.1e-14\%$	$90.8 \pm 1.1e-14\%$
Weighted	Precision	$98.7 \pm 1.1e-14\%$	$98.4 \pm 0\%$	$98.6 \pm 0\%$	$98.8 \pm 0\%$
	Recall	$98.7 \pm 1.1e-14\%$	$98.5 \pm 0\%$	$98.7 \pm 0\%$	$98.8 \pm 0\%$
	F1 score	$98.7 \pm 0\%$	$98.3 \pm 1.1e-14\%$	$98.6 \pm 0\%$	$98.8 \pm 1.1e-14\%$

TABLE 5.4: Average of evaluation metrics of each class after CNN training using 5-fold cross-validation technique. Metrics are exported for GAUS4 and GAUS8 wavelets and each preprocessing method.

		GAUS4		GAUS8	
Class	**Metric**	M	M-N	M	M-N
N	Precision	$99.2 \pm 0\%$	$99.1 \pm 0\%$	$99 \pm 0\%$	$99.1 \pm 0\%$
	Recall	$99.8\% \pm 0$	$99.8 \pm 1.1e-14\%$	$99.8 \pm 1.1e-14\%$	$99.8 \pm 0\%$
	F1 score	$\mathbf{99.5\% \pm 0}$	$99.4 \pm 0\%$	$99.4 \pm 0\%$	$99.4 \pm 1.1e-14\%$
SVEB	Precision	$94.4 \pm 1.1e-14\%$	$93.9 \pm 1.1e-14\%$	$93.7 \pm 1.1e-14\%$	$92.5 \pm 1.1e-14\%$
	Recall	$80.2 \pm 1.1e-14\%$	$79.1 \pm 0\%$	$78.9 \pm 0\%$	$78.7 \pm 0\%$
	F1 score	$86.7 \pm 0\%$	$85.9 \pm 0\%$	$85.7 \pm 1.1e-14\%$	$85 \pm 1.1e-14\%$
VEB	Precision	$97.2 \pm 0\%$	$97.2 \pm 0\%$	$97.6 \pm 0\%$	$97.6 \pm 0\%$
	Recall	$97.6 \pm 0\%$	$97.1 \pm 1.1e-14\%$	$97.6 \pm 0\%$	$97.5 \pm 1.1e-14\%$
	F1 score	$97.4 \pm 1.1e-14\%$	$97.1 \pm 0\%$	$\mathbf{97.6 \pm 0\%}$	$\mathbf{97.6 \pm 0\%}$
Q	Precision	$93.6 \pm 0\%$	$90.2 \pm 0\%$	$91.7 \pm 0\%$	$91.1 \pm 0\%$
	Recall	$71.5 \pm 0\%$	$66.7 \pm 0\%$	$60.6 \pm 0\%$	$67.9 \pm 0\%$
	F1 score	$\mathbf{81.1 \pm 1.1e-14\%}$	$76.7 \pm 0\%$	$73 \pm 0\%$	$77.8 \pm 0\%$

In this study, 5-fold cross-validation was utilized. In terms of F1- score the maximum results taken from this method and for each method are displayed below.

- **N** class:
  The use of only *median* filtering at each record and the *gaus4* mother wavelet to create the coefficients, achieved F1 score of $99.5\% \pm 0.01e-16$.

TABLE 5.5: Average evaluation metrics of GAUS4 & GAUS8 wavelets after CNN training.

		GAUS4		GAUS8	
Class	**Metric**	M	M-N	M	M-N
Macro	Precision	$96.1 \pm 1.1e-14\%$	$95.1 \pm 1.1e-14\%$	$95.5 \pm 1.1e-14\%$	$95.1 \pm 1.1e-14\%$
	Recall	$87.3\% \pm 0$	$85.7 \pm 1.1e-14\%$	$84.2 \pm 0\%$	$86 \pm 0\%$
	F1 score	$91.2\% \pm 0$	$89.8 \pm 0\%$	$88.9 \pm 0\%$	$89.9 \pm 0\%$
Weighted	Precision	$98.8 \pm 1.1e-14\%$	$98.7 \pm 0\%$	$98.7 \pm 1.1e-14\%$	$98.7 \pm 0\%$
	Recall	$98.9 \pm 0\%$	$98.8 \pm 0\%$	$98.8 \pm 0\%$	$98.8 \pm 1.1e-14\%$
	F1 score	$98.8 \pm 1.1e-14\%$	$98.7 \pm 1.1e-14\%$	$98.7 \pm 0\%$	$98.7 \pm 1.1e-14\%$

- **SVEB** class:
  The use of *median and notch* filtering and the *morl* mother wavelet, achieved the maximum F1 score of $87.5\% \pm 0.01e-16$.
- **VEB** class:
  The use of *median* filtering and the *gaus8* wavelet, achieved the maximum F1 score of $97.6\% \pm 0$.
- **Q** class:
  Despite the restricted number of data for this class, the maximum f1 score achieved is $81.1\% \pm 1.12e-16$ with the use of *median* filtering at the preprocessing step and the *gaus4* wavelet at the feature extraction set.

5.1 Outlook

5.1.1 Device Communication and GUIs

Future work for this part should focus on integrating real-time processing capabilities for R peak detection, EDR calculation, and arrhythmia prediction with live data capture. This could be achieved by processing data in short intervals, such as 1 or 2 seconds, allowing the algorithms sufficient time to perform accurate calculations. Additionally, incorporating a database solution, such as SQLite, could be beneficial for storing records efficiently. This database would minimize storage requirements while providing more comprehensive information, such as user-specific health metrics and historical data, thereby facilitating more detailed and personalized analysis.

Moreover, future developments should consider integration with other devices like electroencephalography (EEG) devices or the capability of more ECG devices offering a more comprehensive view of the user's health with a bigger variety of metrics (EEG and/or multi-lead ECG).

Finally, transforming the Raspberry Pi into a node within an internet of things ecosystem. Using cloud-based systems, users can access their health data both locally and online, as well as run more computationally needed tasks like the continuous training of the model used, with the user's data and unique features (patient parading).

5.1.2 Arrhythmia Model Training

For the arrhythmia prediction model, future research should consider incorporating additional arrhythmia types, such as Atrial Fibrillation, for which numerous datasets are readily available online. Expanding the range of arrhythmia types and utilizing larger datasets will enhance the model's robustness and provide a more comprehensive evaluation of its performance. Additionally, testing more complex architectures may be necessary if predicting a greater number of arrhythmia classes. Finally, leveraging cloud computing could facilitate online learning and/or federated learning, further improving the model's capabilities.

Bibliography

[1] Turky N. Alotaiby et al. "ECG-Based Subject Identification Using Common Spatial Pattern and SVM". In: *Journal of Sensors* 2019.1 (2019), p. 8934905. DOI: https://doi.org/10.1155/2019/8934905. eprint: https://onlinelibrary.wiley.com/doi/pdf/10.1155/2019/8934905. URL: https://onlinelibrary.wiley.com/doi/abs/10.1155/2019/8934905.

[2] Apple Inc. *Healthcare - Apple Watch*. 2024. URL: https://www.apple.com/healthcare/apple-watch/.

[3] M. Riadh Arefin, Kouhyar Tavakolian, and Reza Fazel-Rezai. "QRS complex detection in ECG signal for wearable devices". In: *2015 37th Annual International Conference of the IEEE Engineering in Medicine and Biology Society (EMBC)*. 2015, pp. 5940–5943. DOI: 10.1109/EMBC.2015.7319744.

[4] *Arrhythmias - What Is an Arrhythmia? | NHLBI, NIH*. Mar. 2022.

[5] Daniel E Becker. "Fundamentals of Electrocardiography Interpretation". In: *Anesthesia Progress* 53.2 (2006), pp. 53–64. ISSN: 0003-3006. DOI: 10.2344/0003-3006(2006)53[53:FOEI]2.0.CO;2.

[6] Alexandre Bernardino and José Santos-Victor. "Visual Surveillance in a Multi-Camera Environment". In: *Proceedings of the 2nd Iberian Conference on Pattern Recognition and Image Analysis (IbPRIA)*. Accessed: 2024-07-09. 2005, pp. 103–110. URL: https://homepages.inf.ed.ac.uk/rbf/CAVIAR/PAPERS/05-ibpria-alex.pdf.

[7] *Bleak — Bleak 0.22.2 Documentation*. https://bleak.readthedocs.io/en/latest/index.html. (Visited on 07/16/2024).

[8] Gernot Boeck. "Master Thesis: [Specific Title of the Thesis]". MA thesis. Johannes Kepler University Linz, 2019. URL: https://www.jku.at/fileadmin/gruppen/183/Docs/Finished_Theses/Master_Thesis_Boeck.pdf#page=98&zoom=100,176,466.

[9] Jan C. Brammer. "biopeaks: a graphical user interface for feature extraction from heart- and breathing biosignals". In: *Journal of Open Source Software* 5.54 (2020), p. 2621. DOI: 10.21105/joss.02621. URL: https://doi.org/10.21105/joss.02621.

[10] Peter Charlton et al. "An assessment of algorithms to estimate respiratory rate from the electrocardiogram and photoplethysmogram". In: *Physiological measurement* 37 (Mar. 2016), pp. 610–626. DOI: 10.1088/0967-3334/37/4/610.

[11] Raheel Chaudhry, Julia H. Miao, and Afzal Rehman. "Physiology, Cardiovascular". In: *StatPearls*. Treasure Island (FL): StatPearls Publishing, 2024.

[12] Mahesh Chavan, Ra Agarwala, and Mahadev Uplane. "Suppression of noise in the ECG signal using digital IIR filter". In: (Jan. 2008).

[13] Philip Chazal. "Detection of supraventricular and ventricular ectopic beats using a single lead ECG". In: *Conference proceedings : ... Annual International Conference of the IEEE Engineering in Medicine and Biology Society. IEEE Engineering in Medicine and Biology Society. Conference* 2013 (July 2013), pp. 45–48. DOI: 10.1109/EMBC.2013.6609433.

[14] Philip Chazal, Maria O'Dwyer, and Richard Reilly. "Automatic Classification of Heartbeats Using ECG Morphology and Heartbeat Interval Features". In: *IEEE transactions on bio-medical engineering* 51 (Aug. 2004), pp. 1196–206. DOI: 10.1109/TBME.2004.827359.

[15] Philip Chazal, Maria O'Dwyer, and Richard Reilly. "Automatic Classification of Heartbeats Using ECG Morphology and Heartbeat Interval Features". In: *IEEE transactions on bio-medical engineering* 51 (Aug. 2004), pp. 1196–206. DOI: 10.1109/TBME.2004.827359.

[16] Shanshan Chen et al. "Heartbeat classification using projected and dynamic features of ECG signal". In: *Biomedical Signal Processing and Control* 31 (2017), pp. 165–173. ISSN: 1746-8094. DOI: https://doi.org/10.1016/j.bspc.2016.07.010. URL: https://www.sciencedirect.com/science/article/pii/S1746809416300908.

[17] Corsano. *Solutions*. Accessed: 2024-07-23. 2024. URL: https://corsano.com/solutions/.

[18] I. Daubechies. "The wavelet transform, time-frequency localization and signal analysis". In: *IEEE Transactions on Information Theory* 36.5 (1990), pp. 961–1005. ISSN: 1557-9654. DOI: 10.1109/18.57199.

[19] João Paulo do Vale Madeiro et al. "Chapter 3 - Techniques for Noise Suppression for ECG Signal Processing". In: *Developments and Applications for ECG Signal Processing*. Ed. by João Paulo do Vale Madeiro et al. Academic Press, 2019, pp. 53–87. ISBN: 978-0-12-814035-2. DOI: https://doi.org/10.1016/B978-0-12-814035-2.00009-8. URL: https://www.sciencedirect.com/science/article/pii/B9780128140352000098.

[20] João Paulo do Vale Madeiro et al. "Evaluation of mathematical models for QRS feature extraction and QRS morphology classification in ECG signals". In: *Measurement* 156 (2020), p. 107580. ISSN: 0263-2241. DOI: https://doi.org/10.1016/j.measurement.2020.107580. URL: https://www.sciencedirect.com/science/article/pii/S0263224120301172.

[21] Mohamed Elgendi, Mirjam Jonkman, and Friso De Boer. "Frequency Bands Effects on QRS Detection." In: Jan. 2010, pp. 428–431.

[22] Raspberry Pi Foundation. *Raspberry Pi Documentation*. https://www.raspberrypi.com/documentation/. 2024.

[23] "Fourier Transform". In: *Wikipedia* (June 2024). (Visited on 07/03/2024).

[24] J.E. Fowler. "The Redundant Discrete Wavelet Transform and Additive Noise". In: *IEEE Signal Processing Letters* 12.9 (Sept. 2005), pp. 629–632. ISSN: 1558-2361. DOI: 10.1109/LSP.2005.853048. (Visited on 07/05/2024).

[25] G. Garcia et al. "Inter-Patient ECG Heartbeat Classification with Temporal VCG Optimized by PSO". In: *Sci Rep* 7 (2017), p. 10543. DOI: 10.1038/s41598-017-09837-3. URL: https://doi.org/10.1038/s41598-017-09837-3.

[26] Garmin. *Physiological Measurements*. 2024. URL: https://www.garmin.com/en-US/garmin-technology/running-science/physiological-measurements/.

[27] GeeksforGeeks. *Confusion Matrix in Machine Learning*. https://www.geeksforgeeks.org/confusion-matrix-machine-learning/. Accessed: 2024-07-14.

[28] A. Goldberger et al. "PhysioBank, PhysioToolkit, and PhysioNet: Components of a new research resource for complex physiologic signals". In: *Circulation* 101.23 (2000). [Online], e215–e220. URL: https://www.ahajournals.org/doi/10.1161/01.CIR.101.23.e215.

[29] Carles Gomez, Joaquim Oller, and Josep Paradells. "Overview and Evaluation of Bluetooth Low Energy: An Emerging Low-Power Wireless Technology". In: *Sensors (Basel, Switzerland)* 12.9 (Aug. 2012), pp. 11734–11753. ISSN: 1424-8220. DOI: 10.3390/s120911734.

[30] Paul Grossman and Edwin W. Taylor. "Toward understanding respiratory sinus arrhythmia: Relations to cardiac vagal tone, evolution and biobehavioral functions". In: *Biological Psychology* 74.2 (2007). Special Issue of Biological Psychology on Cardiac Vagal Control, Emotion, Psychopathology, and Health., pp. 263–285. ISSN: 0301-0511. DOI: https://doi.org/10.1016/j.biopsycho.2005.11.014. URL: https://www.sciencedirect.com/science/article/pii/S0301051106001876.

[31] P. Hamilton. "Open source ECG analysis". In: *Computers in Cardiology*. 2002, pp. 101–104. DOI: 10.1109/CIC.2002.1166717.

[32] Kaiming He et al. "Delving Deep into Rectifiers: Surpassing Human-Level Performance on ImageNet Classification". In: *Proceedings of the IEEE International Conference on Computer Vision (ICCV)*. 2015.

[33] M.A. Hearst et al. "Support vector machines". In: *IEEE Intelligent Systems and their Applications* 13.4 (1998), pp. 18–28. DOI: 10.1109/5254.708428.

[34] L. Howell and B. Porr. *High precision ECG database with annotated R peaks, recorded and filmed under realistic conditions*. Retrieved July 21, 2024. DOI: 10.5525/gla.researchdata.716. 2018. URL: https://doi.org/10.5525/gla.researchdata.716.

[35] Bosun Hwang et al. "Deep ECGNet: An Optimal Deep Learning Framework for Monitoring Mental Stress Using Ultra Short-Term ECG Signals". In: *Telemedicine and e-Health* 24.10 (2018). PMID: 29420125, pp. 753–772. DOI: 10.1089/tmj.2017.0250. eprint: https://doi.org/10.1089/tmj.2017.0250. URL: https://doi.org/10.1089/tmj.2017.0250.

[36] Plotly Technologies Inc. *Dash Layout*. https://dash.plotly.com/layout. 2024.

[37] Sergey Ioffe and Christian Szegedy. *Batch Normalization: Accelerating Deep Network Training by Reducing Internal Covariate Shift*. 2015. arXiv: 1502.03167 [cs.LG]. URL: https://arxiv.org/abs/1502.03167.

[38] Sergey Ioffe and Christian Szegedy. "Batch Normalization: Accelerating Deep Network Training by Reducing Internal Covariate Shift". In: *Proceedings of the 32nd International Conference on Machine Learning*. Ed. by Francis Bach and David Blei. Vol. 37. Proceedings of Machine Learning Research. Lille, France: PMLR, 2015, pp. 448–456. URL: https://proceedings.mlr.press/v37/ioffe15.html.

[39] Talha Iqbal et al. "A Sensitivity Analysis of Biophysiological Responses of Stress for Wearable Sensors in Connected Health". In: *IEEE Access* PP (Jan. 2021), pp. 1–1. DOI: 10.1109/ACCESS.2021.3082423.

[40] Menghan JIA et al. "High Noise Tolerant R-Peak Detection Method Based on Deep Convolution Neural Network". In: *IEICE Transactions on Information and Systems* E102.D.11 (2019), pp. 2272–2275. DOI: 10.1587/transinf.2019EDL8097.

[41] L. Jian et al. "Classification of ECG Arrhythmia Using CNN, SVM and LDA". In: *Proceedings of the Artificial Intelligence and Security, 5th International Conference, ICAIS 2019*. Vol. 11633. Lecture Notes in Computer Science. New York, NY, USA: Springer, 2019, pp. 191–201. DOI: 10.1007/978-3-030-24265-7_17. URL: https://link.springer.com/chapter/10.1007/978-3-030-24265-7_17.

[42] Selcan Kaplan Berkaya et al. "A survey on ECG analysis". In: *Biomedical Signal Processing and Control* 43 (2018), pp. 216–235. ISSN: 1746-8094. DOI: https://doi.org/10.1016/j.bspc.2018.03.003. URL: https://www.sciencedirect.com/science/article/pii/S1746809418300636.

[43] Anthony H. Kashou, Hajira Basit, and Lovely Chhabra. "Physiology, Sinoatrial Node". In: *StatPearls*. Treasure Island (FL): StatPearls Publishing, 2024.

[44] Alan Kennedy et al. "Automated detection of atrial fibrillation using R-R intervals and multivariate-based classification". In: *Journal of Electrocardiology* 49.6 (2016), pp. 871–876. ISSN: 0022-0736. DOI: https://doi.org/10.1016/j.jelectrocard.2016.07.033. URL: https://www.sciencedirect.com/science/article/pii/S002207361630111X.

[45] Heba Khamis et al. "QRS Detection Algorithm for Telehealth Electrocardiogram Recordings". In: *IEEE Transactions on Biomedical Engineering* 63.7 (2016), pp. 1377–1388. DOI: 10.1109/TBME.2016.2549060.

[46] Vladimír Kunc and Jiří Kléma. *Three Decades of Activations: A Comprehensive Survey of 400 Activation Functions for Neural Networks*. 2024. arXiv: 2402.09092 [cs.LG]. URL: https://arxiv.org/abs/2402.09092.

[47] Bhargav Lenka. "Time-frequency analysis of non-stationary electrocardiogram signals using Hilbert-Huang Transform". In: *2015 International Conference on*

Communications and Signal Processing (ICCSP). 2015, pp. 1156–1159. DOI: 10.1109/ICCSP.2015.7322686.

[48] Chao Lin, Corinne Mailhes, and Jean-Yves Tourneret. "P- and T-Wave Delineation in ECG Signals Using a Bayesian Approach and a Partially Collapsed Gibbs Sampler". In: *IEEE Transactions on Biomedical Engineering* 57.12 (2010), pp. 2840–2849. DOI: 10.1109/TBME.2010.2076809.

[49] Chun-Cheng Lin and Chun-Min Yang. "Heartbeat Classification Using Normalized RR Intervals and Morphological Features". In: *Mathematical Problems in Engineering* 2014.1 (2014), p. 712474. DOI: https://doi.org/10.1155/2014/712474. eprint: https://onlinelibrary.wiley.com/doi/pdf/10.1155/2014/712474. URL: https://onlinelibrary.wiley.com/doi/abs/10.1155/2014/712474.

[50] Mariano Llamedo and Juan Pablo Martinez. "Heartbeat Classification Using Feature Selection Driven by Database Generalization Criteria". In: *IEEE transactions on bio-medical engineering* 58.3 (Mar. 2011), pp. 616–625. ISSN: 1558-2531. DOI: 10.1109/TBME.2010.2068048.

[51] Dominique Makowski et al. "NeuroKit2: A Python toolbox for neurophysiological signal processing". In: *Behavior Research Methods* 53.4 (2021), pp. 1689–1696. DOI: 10.3758/s13428-020-01516-y. URL: https://doi.org/10.3758%2Fs13428-020-01516-y.

[52] Jyotsna Kumar Mandal. "Z-Transform-Based Reversible Encoding". In: *Reversible Steganography and Authentication via Transform Encoding*. Vol. 901. Studies in Computational Intelligence. Singapore: Springer Singapore, 2020, pp. 157–195. ISBN: 978-981-15-4396-8. DOI: 10.1007/978-981-15-4397-5_7.

[53] Association for the Advancement of Medical Instrumentation and American National Standards Institute. *Testing and Reporting Performance Results of Cardiac Rhythm and ST-segment Measurement Algorithms*. ANSI/AAMI. The Association, 1999. ISBN: 9781570201165. URL: https://books.google.gr/books?id=gzPdtgAACAAJ.

[54] Association for the Advancement of Medical Instrumentation. Arrhythmia Monitoring Subcommittee. *Recommended Practice for Testing and Reporting Performance Results of Ventricular Arrhythmia Detection Algorithms (proposed)*. AAMI recommended practice. Association for the Advancement of Medical Instrumentation, 1986. URL: https://books.google.gr/books?id=ojkGHAAACAAJ.

[55] G.B. Moody and R.G. Mark. "The impact of the MIT-BIH Arrhythmia Database". In: *IEEE Engineering in Medicine and Biology Magazine* 20.3 (2001), pp. 45–50. ISSN: 1937-4186. DOI: 10.1109/51.932724.

[56] Movesense. *Movesense Medical MDR*. https://www.movesense.com/product/movesense-medical-mdr/. 2024.

[57] R. Joe Noble, J. Stanley Hillis, and Donald A. Rothbaum. "Electrocardiography". In: *Clinical Methods: The History, Physical, and Laboratory Examinations*.

Ed. by H. Kenneth Walker, W. Dallas Hall, and J. Willis Hurst. 3rd. Boston: Butterworths, 1990. ISBN: 978-0-409-90077-4.

[58] Keiron O'Shea and Ryan Nash. *An Introduction to Convolutional Neural Networks*. 2015. arXiv: 1511.08458 [cs.NE]. URL: https://arxiv.org/abs/1511.08458.

[59] Jiapu Pan and Willis J. Tompkins. "A Real-Time QRS Detection Algorithm". In: *IEEE Transactions on Biomedical Engineering* BME-32.3 (1985), pp. 230–236. DOI: 10.1109/TBME.1985.325532.

[60] Adam Paszke et al. *PyTorch: An Imperative Style, High-Performance Deep Learning Library*. 2019. arXiv: 1912.01703 [cs.LG]. URL: https://arxiv.org/abs/1912.01703.

[61] Sudip Paul et al. "Chapter 1 - Overview of Biomedical Instrumentation". In: *Introduction to Biomedical Instrumentation and Its Applications*. Ed. by Sudip Paul et al. Academic Press, Jan. 2022, pp. 1–43. ISBN: 978-0-12-821674-3. DOI: 10.1016/B978-0-12-821674-3.00010-3.

[62] Christos Pavlatos et al. "HARDWARE IMPLEMENTATION OF PAN & TOMPKINS QRS DETECTION ALGORITHM". In: ().

[63] Fabian Pedregosa et al. *Scikit-learn: Machine Learning in Python*. 2018. arXiv: 1201.0490 [cs.LG]. URL: https://arxiv.org/abs/1201.0490.

[64] Tam Pham et al. "Heart Rate Variability in Psychology: A Review of HRV Indices and an Analysis Tutorial". In: *Sensors* 21.12 (2021). ISSN: 1424-8220. DOI: 10.3390/s21123998. URL: https://www.mdpi.com/1424-8220/21/12/3998.

[65] Jacek Piskorowski. "Powerline interference removal from ECG signal using notch filter with non-zero initial conditions". In: *2012 IEEE International Symposium on Medical Measurements and Applications Proceedings*. 2012, pp. 1–3. DOI: 10.1109/MeMeA.2012.6226635.

[66] Bernd Porr and Luis Howell. *R-peak detector stress test with a new noisy ECG database reveals significant performance differences amongst popular detectors*. Aug. 2019. DOI: 10.1101/722397.

[67] J. Rafiee, M.A. Rafiee, and P.W. Tse. "Application of mother wavelet functions for automatic gear and bearing fault diagnosis". In: *Expert Systems with Applications* 37.6 (2010), pp. 4568–4579. ISSN: 0957-4174. DOI: https://doi.org/10.1016/j.eswa.2009.12.051. URL: https://www.sciencedirect.com/science/article/pii/S0957417409010975.

[68] *Regulation (EU) 2017/745 of the European Parliament and of the Council of 5 April 2017 on Medical Devices, Amending Directive 2001/83/EC, Regulation (EC) No 178/2002 and Regulation (EC) No 1223/2009 and Repealing Council Directives 90/385/EEC and 93/42/EEC (Text with EEA Relevance.)* Apr. 2017. URL: https://eur-lex.europa.eu/legal-content/EN/TXT/?uri=CELEX%3A32017R0745.

[69] Ibraheem Rehman and Afzal Rehman. "Anatomy, Thorax, Heart". In: *StatPearls*. Treasure Island (FL): StatPearls Publishing, 2024.

[70] Tiago Rodrigues et al. "A Low-Complexity R-peak Detection Algorithm with Adaptive Thresholding for Wearable Devices". In: Jan. 2021. DOI: 10.1109/ICPR48806.2021.9413245.

[71] Bruce Rogers et al. "The Movesense Medical Sensor Chest Belt Device as Single Channel ECG for RR Interval Detection and HRV Analysis during Resting State and Incremental Exercise: A Cross-Sectional Validation Study". In: *Sensors* 22.5 (Jan. 2022), p. 2032. ISSN: 1424-8220. DOI: 10.3390/s22052032.

[72] Harold Ryan. *Choice of Wavelets*. Accessed: 2024-07-09. 1994. URL: https://web.archive.org/web/20141227215059/http://74.3.176.63/publications/recorder/1994/09sep/sep94-choice-of-wavelets.pdf.

[73] Samsung. *Samsung Health Monitor*. 2024. URL: https://www.samsung.com/us/apps/samsung-health-monitor/.

[74] Surita Sarkar, Saptak Bhattacherjee, and Saurabh Pal. "Extraction of respiration signal from ECG for respiratory rate estimation". In: *Michael Faraday IET International Summit 2015*. 2015, pp. 336–340. DOI: 10.1049/cp.2015.1654.

[75] Mark S Schwartz and Frank Andrasik. *Biofeedback: A practitioner's guide*. New York: The Guilford Press, 2016, pp. 196–213.

[76] I.W. Selesnick and C.S. Burrus. "Generalized digital Butterworth filter design". In: *IEEE Transactions on Signal Processing* 46.6 (1998), pp. 1688–1694. DOI: 10.1109/78.678493.

[77] Fred Shaffer and J. P. Ginsberg. "An Overview of Heart Rate Variability Metrics and Norms". In: *Frontiers in Public Health* 5 (Sept. 2017), p. 258. ISSN: 2296-2565. DOI: 10.3389/fpubh.2017.00258. (Visited on 07/08/2024).

[78] Fred Shaffer and Jayson P. Ginsberg. "Heart rate variability: standards of measurement, physiological interpretation, and clinical use". In: *Frontiers in Psychology* 5 (2017), p. 1043. URL: https://www.ncbi.nlm.nih.gov/pmc/articles/PMC4311559/.

[79] Mallat Stéphane. "CHAPTER 4 - Time Meets Frequency". In: *A Wavelet Tour of Signal Processing (Third Edition)*. Ed. by Mallat Stéphane. Third Edition. Boston: Academic Press, 2009, pp. 89–153. ISBN: 978-0-12-374370-1. DOI: https://doi.org/10.1016/B978-0-12-374370-1.00008-2. URL: https://www.sciencedirect.com/science/article/pii/B9780123743701000082.

[80] Mallat Stéphane. "CHAPTER 6 - Wavelet Zoom". In: *A Wavelet Tour of Signal Processing (Third Edition)*. Ed. by Mallat Stéphane. Third Edition. Boston: Academic Press, 2009, pp. 205–261. ISBN: 978-0-12-374370-1. DOI: https://doi.org/10.1016/B978-0-12-374370-1.00010-0. URL: https://www.sciencedirect.com/science/article/pii/B9780123743701000100.

[81] Mallat Stéphane. "CHAPTER 7 - Wavelet Bases". In: *A Wavelet Tour of Signal Processing (Third Edition)*. Ed. by Mallat Stéphane. Third Edition. Boston: Academic Press, 2009, pp. 263–376. ISBN: 978-0-12-374370-1. DOI: https://doi.org/10.1016/B978-0-12-374370-1.00011-2. URL: https://www.sciencedirect.com/science/article/pii/B9780123743701000112.

[82] Mallat Stéphane. "CHAPTER 8 - Wavelet Packet and Local Cosine Bases". In: *A Wavelet Tour of Signal Processing (Third Edition)*. Ed. by Mallat Stéphane. Third Edition. Boston: Academic Press, 2009, pp. 377–434. ISBN: 978-0-12-374370-1. DOI: https://doi.org/10.1016/B978-0-12-374370-1.00012-4. URL: https://www.sciencedirect.com/science/article/pii/B9780123743701000124.

[83] Mallat Stéphane. "CHAPTER 9 - Approximations in Bases". In: *A Wavelet Tour of Signal Processing (Third Edition)*. Ed. by Mallat Stéphane. Third Edition. Boston: Academic Press, 2009, pp. 435–480. ISBN: 978-0-12-374370-1. DOI: https://doi.org/10.1016/B978-0-12-374370-1.00013-6. URL: https://www.sciencedirect.com/science/article/pii/B9780123743701000136.

[84] MP Tarvainen et al. "Kubios HRV Version 3–user's guide". In: *Kuopio: University of Eastern Finland* (2017).

[85] Karl Thurnhofer-Hemsi et al. *Radial basis function kernel optimization for Support Vector Machine classifiers*. 2020. arXiv: 2007.08233 [cs.LG]. URL: https://arxiv.org/abs/2007.08233.

[86] Ilya Tolstikhin et al. *MLP-Mixer: An all-MLP Architecture for Vision*. 2021. arXiv: 2105.01601 [cs.CV]. URL: https://arxiv.org/abs/2105.01601.

[87] Christopher Torrence and Gilbert P. Compo. "A Practical Guide to Wavelet Analysis". In: *Bulletin of the American Meteorological Society* 79.1 (Jan. 1998), pp. 61–78. ISSN: 0003-0007, 1520-0477. DOI: 10.1175/1520-0477(1998)079<0061:APGTWA>2.0.CO;2.

[88] Paul van Gent et al. "HeartPy: A novel heart rate algorithm for the analysis of noisy signals". In: *Transportation Research Part F: Traffic Psychology and Behaviour* 66 (2019), pp. 368–378. ISSN: 1369-8478. DOI: https://doi.org/10.1016/j.trf.2019.09.015. URL: https://www.sciencedirect.com/science/article/pii/S1369847818306740.

[89] Tao Wang et al. "Automatic ECG Classification Using Continuous Wavelet Transform and Convolutional Neural Network". In: *Entropy* 23.1 (2021). ISSN: 1099-4300. DOI: 10.3390/e23010119. URL: https://www.mdpi.com/1099-4300/23/1/119.

[90] Lance Williams. *Aliasing and Anti-Aliasing: Introduction to Fourier Transforms*. 2001. URL: https://www.cs.unm.edu/~williams/cs530/arfgtw.pdf.

[91] Martin Woolley. "The Bluetooth® Low Energy Primer". In: ().

[92] Ziqian Wu et al. "A Novel Method to Detect Multiple Arrhythmias Based on Time-Frequency Analysis and Convolutional Neural Networks". In: *IEEE Access* 7 (2019), pp. 170820–170830. DOI: 10.1109/ACCESS.2019.2956050.

[93] C. Ye, B. V. Kumar, and M. T. Coimbra. "Heartbeat Classification Using Morphological and Dynamic Features of ECG Signals". In: *IEEE Trans Biomed Eng* 59.10 (2012), pp. 2930–2941. ISSN: 0018-9294. DOI: 10.1109/TBME.2012.2213253.

[94] Fei Zhang, Jun Tan, and Yong Lian. "An Effective QRS Detection Algorithm for Wearable ECG in Body Area Network". In: *2007 IEEE Biomedical Circuits and Systems Conference*. 2007, pp. 195–198. DOI: 10.1109/BIOCAS.2007.4463342.

[95] Z. Zhang et al. "Heartbeat Classification Using Disease-Specific Feature Selection". In: *Comput Biol Med* 46 (Mar. 2014), pp. 79–89. DOI: 10.1016/j.compbiomed.2013.11.019. URL: https://doi.org/10.1016/j.compbiomed.2013.11.019.